DESIGN, FABRICATION, AND TESTING OF

A VARIABLE FOCUSING MICROMIRROR ARRAY LENS

A Dissertation

by

GYOUNGIL CHO

Submitted to the Office of Graduate Studies of
Texas A&M University
in partial fulfillment of the requirements for the degree of

DOCTOR OF PHILOSOPHY

May 2004

Major Subject: Aerospace Engineering

DESIGN, FABRICATION, AND TESTING OF A VARIABLE FOCUSING MICROMIRROR ARRAY LENS

A Dissertation

by

GYOUNGIL CHO

Submitted to Texas A&M University
in partial fulfillment of the requirements
for the degree of

DOCTOR OF PHILOSOPHY

Approved as to style and content by:

James G. Boyd
(Chair of Committee)

Johnny Hurtado
(Member)

Kenneth D. Kihm
(Member)

Won-jong Kim
(Member)

Walter E. Haisler
(Head of Department)

Major Subject: Aerospace Engineering

ABSTRACT

Design, Fabrication, and Testing of

a Variable Focusing Micromirror Array Lens. (May 2004)

Gyoungil Cho, B.S., Sungkyunkwan University, Suwon, Korea;

M.S., Korea Advanced Institute of Science and Technology, Daejon, Korea;

Ph.D., University of Illinois at Chicago

Chair of Advisory Committee: Dr. James G. Boyd

A reflective type Fresnel lens using an array of micromirrors is designed and fabricated using the MUMPs® surface micromachining process. The focal length of the lens can be rapidly changed by controlling both the rotation and translation of electrostatically actuated micromirrors. The suspension spring, pedestal and electrodes are located under the mirror to maximize the optical efficiency. The micromirror translation and rotation are plotted versus the applied voltage. Relations are provided for the fill-factor and the numerical aperture as functions of the lens diameter, the mirror size, and the tolerances specified by the MUMPs® design rules. Linnik interferometry is used to measure the translation, rotation, and flatness of a fabricated micromirror. The reflective type Fresnel lens is controlled by independent DC voltages of 16 channels with a 0 to 50V range, and translational and torsional stiffness are calibrated with measured data. The spot diameter of the point source by the fabricated and electrostatically controlled reflective type Fresnel lens is measured to test focusing quality of the lens.

To my mom and wife

ACKNOWLEDGMENTS

It was very fortunate that I met my advisor, Dr. James G. Boyd, when I came to Texas A&M University. I thank him for providing invaluable guidance, advice, and support. Whenever I had a problem, he gave me a way and advice to solve it, whatever it was. I sincerely give my best regards to him.

My thanks also go to Dr. Hurtado, Dr. Kihm, and Dr. Kim for helping me as committee members. Dr. Hurtado helped me to enlarge my knowledge of dynamics and mechanics. Dr. Kihm instructed me in optics. Dr. Kim helped me to understand and study the mechatronics.

I would like to thank my elder sister's family and my younger brother's family. Also, I thank my mother-in-law and extended family. They have believed in me and have given me their concern and love to overcome any difficulty.

I am deeply grateful to my father and mother for their endless love and support. Special thanks to my beloved, Mihyun Kwon, and my children, Jimmy and Cameron, for their love, patience, and encouragement. I hope all of them keep in mind that I will always be with them with all my heart.

TABLE OF CONTENTS

CHAPTER		Page
I	INTRODUCTION	1
II	OPTICAL DESIGN	5
	2.1 Imaging principle	5
	2.2 Principle of the micromirror array lens (MMAL)	6
	2.3 Optical design	8
	2.4 Optical simulation	14
III	ELECTRO-MECHANICAL DESIGN	16
	3.1 Overview of static characteristics of phase modulation micromirror	16
	3.2 Structure of the micromirror of MMAL	19
	3.3 Electrostatic force and torque	21
	3.4 Elastic recovery force and torque	23
	3.5 Static behavior	24
	3.6 Stability	27
IV	FABRICATION	28
	4.1 MUMPs technology	28
	4.2 Micromirror fabrication using MUMPs	31
	4.3 Post processing	40
V	EXPERIMENT	43
	5.1 Measurement	43
	5.2 Control and package	50
VI	RESULTS	53
	6.1 Measurement results	53
	6.2 Optical performance	59
VII	CONCLUSIONS	62
REFERENCES		65
APPENDIX A		69
VITA		72

LIST OF FIGURES

FIGURE Page

2.1 Schematic cut-away diagrams of Fresnel lens 6

2.2 Imaging by micromirror array lens 7

2.3 2-D view of the micromirror array lens 8

2.4 Relation between rotation angle of micromirror and specifications of the lens 10

2.5 Loss of effective area by electrode leads 12

2.6 Schematic of optical simulation 14

2.7 Huygens point spread function by micromirror array lens 14

3.1 Schematic view of an electrostatically driven phase modulation micromirror...... 16

3.2 Displacement behavior of the upper plate of a capacitor 18

3.3 Schematic 3-D view of the micromirror and electrode shape 18

3.4 Electrode pair of circular shape 19

3.5 Translation by bending of a suspension spring 20

3.6 Cross-sectional view of the micromirror 20

3.7 Schematic view of a micromirror with translational and rotational displacement 22

3.8 Simulated plot of inside voltage versus translation and rotation 25

3.9 Simulated plot of outside voltage versus translation and rotation 25

3.10 Simulated plot of the gradient of inside voltage versus translation and rotation... 26

4.1 Cross-sectional view of the micromirror fabricated by MUMPs 29

4.2 Three different cross sectional views of the micromirror 31

4.3 The UV-sensitive photoresist 31

FIGURE Page

4.4 The lithographically patterned photoresist to remove unwanted Poly 0 layer....... 32

4.5 The Poly 0 layer patterned by reactive ion etching (RIE) 33

4.6 A 2.0µm layer of PSG by low pressure chemical vapor deposition (LPCVD) 33

4.7 The dimples with 750nm deep by RIE 33

4.8 The oxide layer patterned by RIE... 34

4.9 A blanket 2.0µm layer of Poly 1 deposited by LPCVD 34

4.10 Poly 1 layer patterned by RIE.. 35

4.11 The second oxide layer, 0.75µm of PSG 35

4.12 The second oxide layer patterned by RIE.. 36

4.13 A blanket 1.5µm layer of Poly 2 deposited by LPCVD 36

4.14 Poly 2 layer patterned by RIE.. 37

4.15 The micromirror released by immersing the chips in a 48% HF solution 37

4.16 The lead disconnected by Siloxide 40

4.17 The fabricated micromirror array lens (MMAL) 41

4.18 The leads of micromirror array lens... 41

5.1 Photograph of measurement set-up.. 43

5.2 Linnik interferometry to measure translation, rotation and flatness 44

5.3 Fringe pattern by a spherical object and reference mirror 46

5.4 Equally spaced fringes by pre-tilting between the reference and object mirror 46

5.5 Shifting of fringe pattern by pure translation... 47

5.6 Shifting of the interference fringes by translation 47

5.7 Change of a fringe pitch by rotation of the micromirror 49

5.8 Interference fringes by rotational motions according to the applied voltages 49

FIGURE Page

5.9 Schematic diagram of multi-channel high voltage control system 51

5.10 Photograph of control system 51

5.11 Photograph of MMAL packaged by DIP.. 52

6.1 Plot of the voltage versus translation 53

6.2 Gradient of the voltage, 3μm gap and a reduced translational spring constant 54

6.3 Plot of the voltage versus rotation 54

6.4 Flatness measurement by fringe deformation 55

6.5 Uniformity of angular rotation, 8th micromirrors, 27V.. 56

6.6 Non-uniformity of micromirror rotation at same radius 56

6.7 Set-up for spot diameter measurement... 59

6.8 Spot diameter by MMAL with NA 0.0136.. 60

6.9 Image of real object imaged by the MMAL 61

LIST OF TABLES

TABLE Page

2.1 Requirements for a diffraction-limited micromirror array lens 10

2.2 Fill-factor and maximum numerical aperture of a 1.8mm diameter micromirror array lens for width of single mirror... 13

3.1 Mechanical properties and dimensions of a spring for a micromirror furthest from the lens center... 23

4.1 Structural and sacrificial layers used in MUMPs 28

6.1 Summary of the reasons causing aberration and the rate of aberrations............... 58

6.2 Necessary displacement, displacement error and necessary voltages for MMAL with focal length 33mm 58

A.2.1 Distribution of energy in the diffraction pattern at the focus of a perfect lens as a function of the distance Z from the pattern center(Smith, 1965)................... 71

CHAPTER I

INTRODUCTION

Variable focusing lenses have many applications, including an optical zoom, autofocus, real-time accurate positioning of laser beams, all-in-focus imaging on three-dimensional objects and optical measurement of moving or stationary fields [1-3]. Conventional variable focusing systems using two refractive lenses use complex driving mechanisms to control the relative position of refractive lenses and they have a slow response time. Alternatively, variable focusing lenses have been made [4]. Variable focusing lenses can be made by changing the shape of the lens, as is found in the human eye; this method has been used in lenses made with isotropic liquids [5-7]. The range of numerical aperture (NA) is chosen as a metric of the lenses as well as the range of focal lengths since it gives an idea of how much deflection can be introduced by the lens. Other lenses have been made using electrically variable refractive index media to create either a conventional lens or a gradient index lens by means of a voltage gradient. The electrically variable refractive index then allows the focal length of the lenses to be voltage controlled. One such method uses completely solid electro-optic materials, e.g. $LiTaO_3$ [8] and PLZT [9]. These lenses have a faster response than nematic liquid crystals, e.g. 2.5μs for PLZT [9] compared to 10 – 100ms for a 5μm nematic layer [10]. However, the low electro-optic coefficients (r_{33}=30.8×10^{-12}m^2/V^2 for $LiTaO_3$ [11] and r_{33}=3.6×10^{-16}m^2/V^2 for PLZT [9]) result in small optical path modulation unless thick devices and very large voltages can be tolerated. The potential to form switchable/controllable lenses using the controllable birefringence of liquid crystals was recognized in the 1970's. Originally, the idea of using nematic liquid crystals

---

This dissertation follows the style and format of *Sensors and Actuators.*

to form a liquid crystal lens was proposed and patented by Berreman [12] and investigated by Sato [13]. Various applications were proposed (adaptive spectacles, optics for scanning systems, camera focusing lens) [13-15]. However, the liquid crystal response time increases with the square of the thickness of the cell [10] and with thicker cells it is harder to maintain the crystal structure. The cell thickness used by Sato at the thickest part of the lens was >200μm and the problems associated with a thick liquid crystal cell prohibited serious development. An acceptable switching speed can be achieved by keeping the cell thin (e.g. 5μm, typical of modern LCDs, gives 10–100ms [10]). Unfortunately, thin layers provide little optical path modulation ($\Delta n \cdot d$ = 60μm is achieved with a relatively thick layer: d = 200μm with Δn = 0.3). Therefore, very low numerical apertures and very little change in focusing power when a voltage is applied to the liquid crystal. In order to avoid the problems of the thicker cell, Sato et al. made smaller lenses (microlenses) [16]. They did this by using the edge effects of electrodes patterned with holes to create an electric field, which drops off towards the center of the holes, causing the liquid crystal to form a graded index lens. They found the largest NA was achieved with a diameter to cell thickness ratio of 3:1. This has the advantage over a liquid crystal immersed surface relief structure that the substrates can be flat (which makes the liquid crystal alignment easier), but the cells are still relatively thick (40–100μm in [17]) which will result in slow switching times. Kowel et al. [18] have also used a patterned electrode with liquid crystals to form a lens, but instead of using edge effects to create their non-uniform electric field, they patterned the electrodes to give different voltages in different places. This still only achieved very low numerical apertures (NA. 0.001) and required a system to control the voltages to all the electrodes. Riza et al. [19] used a resistive chain to form the voltage gradient in the electrodes. However, still the numerical aperture achieved was very small (0.004). Naumov et al. [20] used the active impedance of a high resistance control electrode and the liquid crystal cell capacitance

to provide a distribution of a.c. voltage over the area of the liquid crystal lens. A numerical aperture of 0.01 was achieved. A different way to avoid the necessity for a thick cell is to use lenses divided into zones (i.e. a diffractive or Fresnel lens). A diffractive structure immersed in liquid crystal has been tried [21-23]. However, this then loses the variability of focal length. Instead the focal length can be switched between values. If the structure is formed on a programmable phase SLM(spatial light modulator), more flexibility is obtained but only long focal lengths (NA. 0.009) are achievable due to the finite pixel size [1]. A Fresnel lens has also been tried which works by refraction [24], but this had a slow response time (≈3s) since the maximum cell thickness was still relatively large (50μm). A deformed helix ferroelectric liquid crystal has also been used to make a liquid crystal (cylindrical) lens, which had the advantage of a faster response time (20μs for a cell gap of 12μm) than nematic liquid crystals (maximum response time 10ms for a cell gap of 3.4μm) [25]. However, the focal line had several significant side-lobes (≈1/3 of the peak intensity).

The objective of the current research is to develop a variable focusing micromirror array lens (MMAL) satisfying a fast response, large NA, and large diameter. The lens is a variable focusing lens with a fast response time on the order of several tens kHz [26-27]. A large NA can be achieved by increasing the rotational angle of micromirrors. A large diameter lens is possible without losing the optical performance. Because a MMAL consists of a discrete single mirror array, the increasing of lens diameter does not cause a loss of optical performance.

The MMAL uses an array of electrostatically actuated micromirrors. Controlling both the rotation and translation of electrostatically actuated micromirrors can rapidly change the focal length of the lens. Many types of micromirrors or micromirror arrays have been studied and proposed in order to obtain the optimal performance according to their purposes. Among these, vertically moving translational micromirrors and torsional micromirrors have been extensively

used for adaptive optics and beam steering. Therefore, many studies have examined the behavior of an electrostatically deflectable micromirror and described the application of FEM modeling to predict the characteristics of the device [28-29]. The electrostatic behavior of the micromirror was computed and compared with an analytical model and with deflection measurements. In addition, the dynamic behavior of a micromirror as a function of air pressure was presented and compared with the squeeze-film theory [30-32].

Chapter II presents the optical design of MMAL. The required range and accuracy of the mirrors required to make a diffraction-limited lens is presented and the fill-factor and approximation error are calculated. And then, an optical simulation is conducted to test the feasible optical performance of the MMAL. Static behavior of the designed micromirror is analyzed in Chap III. A translational and torsional stiffness and an electrostatic force and torque are calculated to analyze the characteristics in both cases of operation. Because a micromirror has a rotational displacement, a force and torque applied to a micromirror is calculated by regarding mirror plate as being composed of an infinite number of infinitesimally small capacitors. Chap IV introduces a MUMPs process and shows a detailed fabrication procedure for the designed micromirror. To measure the static behavior and flatness of the fabricated micromirror, Chap V shows a measurement system and explains measuring methods for translation, rotation and flatness. Chap VI shows results measured by the system suggested in Chap V, the calibrated static behavior of a micromirror, and optical performance of the MMAL. Finally, the concluding remarks are presents in Chapter VII.

CHAPTER II

OPTICAL DESIGN

2.1 Imaging principle

The purpose of a general lens is to control the light rays. The simplest kind of lens is a pinhole in a piece of thin metal or black paper. Only an extremely small part of the light reflected by an object passes through the pinhole. When the pinhole is large, it allows more light rays to enter but blurs the image. This blur is really an overlapping of several images. Images produced by large and small pinholes are the same size, but one is blurred, while the other is sharp. A refractive lens is a piece of polished and carefully shaped glass that refracts light rays so an image of a desired scene is formed on the rear wall of a lens. A lens transmits more light than a pinhole. It increases the brightness and improves the sharpness of an image. The basic principle of a lens is simple. When the first image formed with a single pinhole and the second image by another pinhole above the first can be made to coincide, the result will be an image twice as bright as the original if the phase of two light rays is the same. Now, consider a third pinhole on the side of the first, a fourth on the other side, and a fifth below the first. All four pinholes project separate images slightly removed from the first or center one. When these four images are made to coincide with the center one, the result is an image five times as bright as the image made by the one center pinhole. By using the principle of refraction or reflection, one can make these four images coincide with the center one. By placing a prism or mirror behind each pinhole, light can be converged, has a same phase and makes a single image. A lens represents a series of prisms incorporated in a single circular piece of glass.

2.2 Principle of the micromirror array lens (MMAL)

In order to obtain a bright and sharp image, all rays leaving one point of an object must converge with the same phase to one point on an image plane. The purpose of a lens is to converge the rays scattered by an object and make each ray have the same optical path length (OPL). Alternatively, the imaging can be achieved by giving each ray the same periodical phase, even though the rays have different OPLs, by adjusting the OPL difference to be integer multiples of the wavelength, λ. Fig. 2.1 shows a schematic cut-away diagram of a Fresnel lens

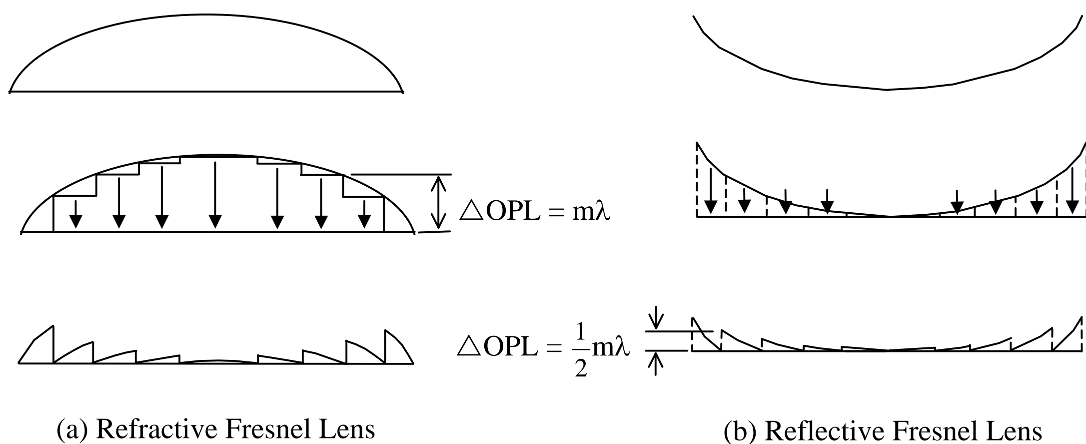

Fig. 2.1. Schematic cut-away diagrams of Fresnel lens

and the micromirror array lens (MMAL), which are similar in principle. Each facet converges rays to one point and rays refracted or reflected by different facets have an OPL difference of integer multiples of λ.

As shown in Fig. 2.2, the rotation of each micromirror is controlled to converge rays and the translation is controlled to adjust the OPL difference to be same phase for each ray:

$$OPL_m - OPL_n = k\lambda \tag{2.1}$$

where m and n are arbitrary indices, k is an integer and λ is the wavelength of the (necessarily) monochromatic light.

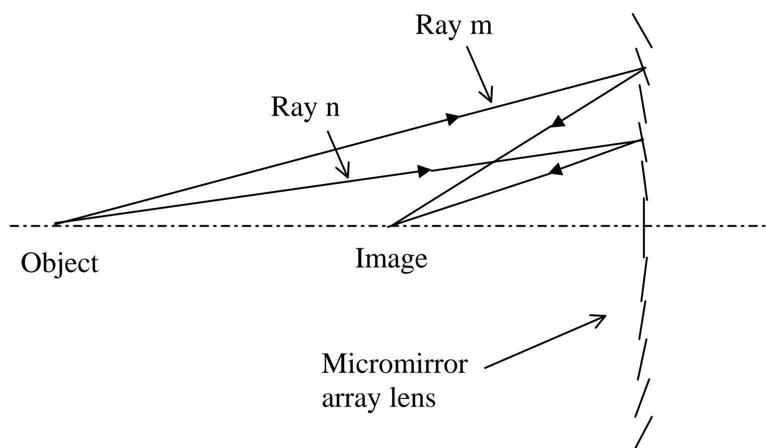

Fig. 2.2. Imaging by micromirror array lens

2.3 Optical design

A 2-D view of the MMAL is shown in Fig 2.3. The lens diameter is 1.8mm, and a polar array of micromirrors is used. It has been demonstrated that a polar array performs better than a rectangular array in removing aberrations [33-35]. The arrays of [34] were fabricated using a flip-chip method by which the upper layers (the mirrors) of the array are fabricated on a separate chip and then transferred to a receiving module containing the lower layers, which includes the address wiring, address electrodes, probe pads, and lower flip-chip bonding structures. The piston-type (translation) array had a very high fill-factor of 98.3%. Rotational mirror arrays demonstrated stable operation through as much as six degrees of rotation. The mirrors in [34] did not have combined translation and rotation, perhaps because they were designed for adaptive optics. In contrast, the MMAL requires both rotational and a translational motion.

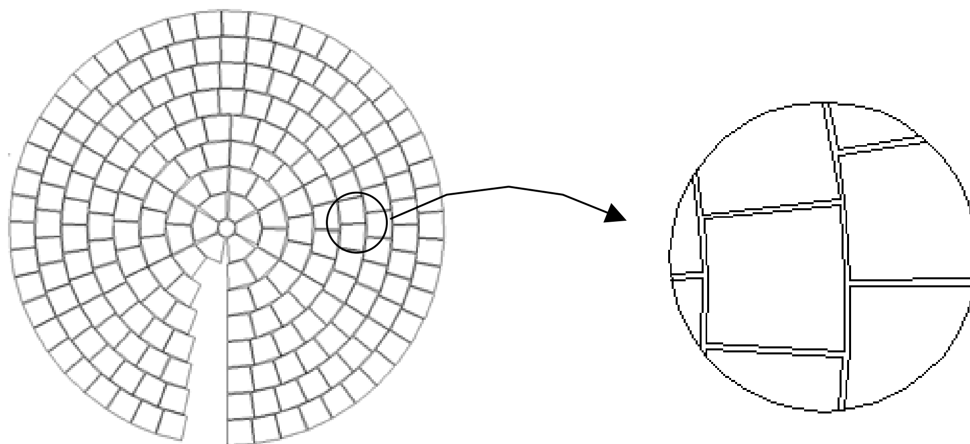

Fig. 2.3. 2-D view of the micromirror array lens

At a given radial position, each mirror has the same shape because the lens is axisymmetric. Each mirror is 100μm wide in the radial direction, and the circumferential dimension is specified such that each mirror has an area of 10,000μm^2. The mirror size and shape at each radial position is designed to increase the effective area for optical efficiency and to decrease the approximation error between the ideal curved shape of a reflective lens and flat surface shape of mirror.

The mirrors must meet range and accuracy requirements to make a diffraction-limited lens (Table 2.1). Electrostatic actuation is used for both translation and rotation. Studies of electrostatically actuated micromirrors demonstrate that mirrors fabricated by surface micromachining satisfy the requirements for a diffraction-limited lens [36-38]. Each mirror is translated to adjust the OPL, and the required translation range is λ/2 because the lens is a reflective type and the phase is periodic. The rotation angle of each micromirror is controlled to converge the rays. The required range of angle depends on the required maximum numerical aperture (NA) of the lens. The relation between the maximum angle and the maximum NA is shown in Fig. 2.4. When the object is in focus, the micromirrors farthest from the center of the lens always have the largest angle. The angular aperture, θ_{max}, is 2 times the maximum rotation angle, α_{max}. Given the definition NA ≡ n sinθ_{max}, the relation between the maximum NA, NA_{max}, and α_{max} is

$$NA_{max} \equiv n \cdot \sin(2\alpha_{max}) \quad (2.2)$$

where n is the refractive index. When θ_{max} is very small, Eq. (2.2) can be approximated as

Table. 2.1. Requirements for a diffraction-limited micromirror array lens

	Requirements for a diffraction-limited micromirror array lens
Range of translation	$\geq \lambda/2$
Accuracy of translation	$< \lambda/8$
Range of angle	$\frac{1}{2}\sin^{-1}\left(\frac{NA_{max}}{n}\right)$
Accuracy of angle	$< 0.091°$
Flatness	$< \lambda/8$

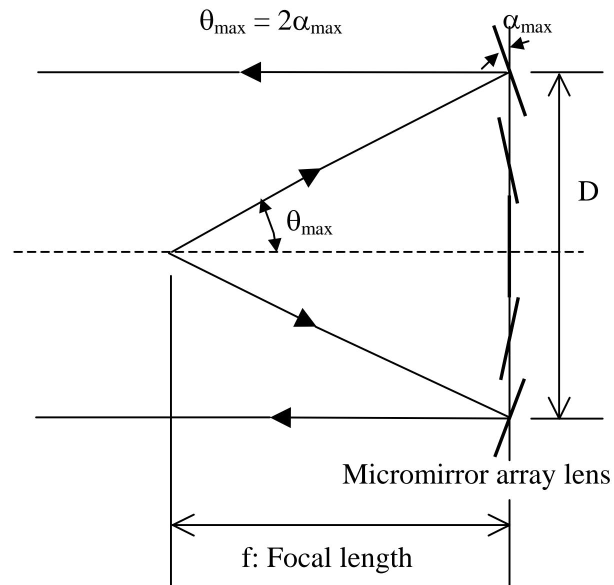

Fig. 2.4. Relation between rotation angle of micromirror and specifications of the lens

$$NA_{\max} = n \cdot \frac{D}{2f} \quad (2.3)$$

The minimum focal length, f_{min}, of the lens is determined by maximum angle from Eq. (2.3):

$$f_{\min} = \frac{D}{4\alpha_{\max}} \tag{2.4}$$

Therefore, the focal length of the lens ranges from f_{min} to infinity. α_{max} is determined by the radial mirror width, *a*, and the thickness, 2μm, of the oxide sacrificial layer used in the MUMPs® process. For this condition, NA_{max} is given by Eqs. (2.3) and (2.4) as

$$NA_{\max} = \frac{8n}{a} \tag{2.5}$$

Because we have chosen *a* to be 100 μm, α_{max} is 2.29° and NA_{max} is 0.080. The focal length of the 1.8mm diameter lens changes from 11.3mm to infinity. As a practical matter, NA_{max} is only 0.0377 because the maximum stable rotation is limited to 1.08° (see section VI).

The maximum aberration for a diffraction-limited lens should be less than λ/4. Therefore, the translation error and flatness error of the mirror surface should be less than λ/8 because this is a reflective type lens. The approximation error is the maximum difference between the position of a point on a conventional Fresnel lens and the position of a corresponding point on the MMAL. This difference arises because the conventional Fresnel lens had curved facets, whereas the micromirrors are nominally flat. The maximum approximation error of a MMAL with a focal

length 25mm and 100μm wide mirrors is 25nm, which is less than λ/8. Therefore, the MMAL can be a diffraction-limited lens.

Angular errors also cause aberrations. The maximum aberration due to angular error occurs at the radial end of each mirror. For λ=632.8nm, an angular accuracy of 0.091° is required to make a diffraction-limited lens because the radial distance from the torsion beam to the end of a mirror is 50μm, i.e. tan 0.091 = 0.6328/(8x50). If the mirror width is increased, an angular accuracy better than 0.091° will be required for λ = 632.8nm. The lens fill-factor, *F*, which is the area fraction of the lens that is covered by mirrors, is given by

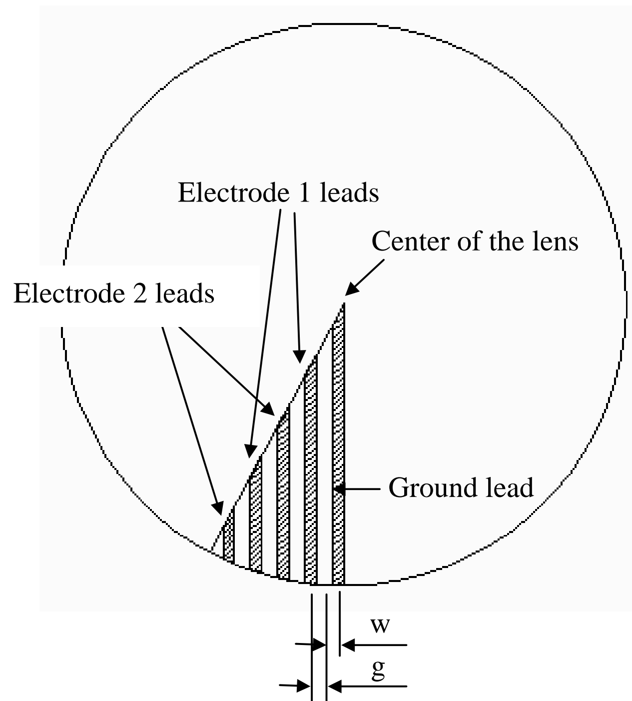

Fig. 2.5. Loss of effective area by electrode leads

$$F = \left(1 - \frac{w+g}{\pi(a+b)}\right) \cdot \left(\frac{a}{a+b}\right)^2 \tag{2.6}$$

where a is the width of single mirror, b is the distance between the mirrors, w is the width of the electrode lead wire, and g is the distance between electrode wires. In deriving Eq. (2.6) it is assumed that each mirror is a square of width a and that the area of the leads and the spaces between the leads is a right triangle (Fig. 2.5), and that the number of circumferential mirror groups is equal to D/(2(a + b)). The minimum b, w, and g are determined by the MUMPs® process, which specifies a minimum feature size of 2μm and a minimum distance between features of 2μm. For the current design, a = 100μm, b = 4μm, w = 3μm, and g = 4μm, and F = 90%. Table. 2.2 shows the fill-factor and maximum numerical aperture for several different values of the mirror width, a.

Table. 2.2. Fill-factor and maximum numerical aperture of a 1.8mm diameter micromirror array lens for width of single mirror

Width of single mirror (μm)	Fill-factor (%)	NA_{max}
20	63	0.4
50	82	0.16
100	90	0.08
200	95	0.04
500	98	0.016

2.4 Optical simulation

An optical simulation software(ZEMAX) was used to model the Strehl ratio and spot

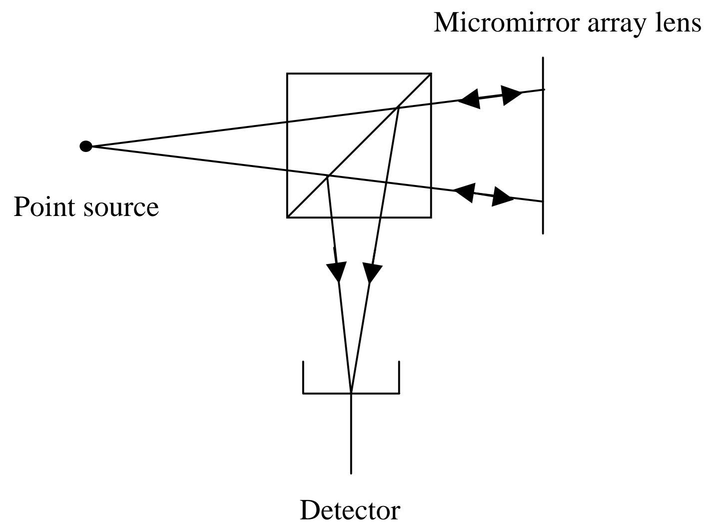

Fig. 2.6. Schematic of optical simulation

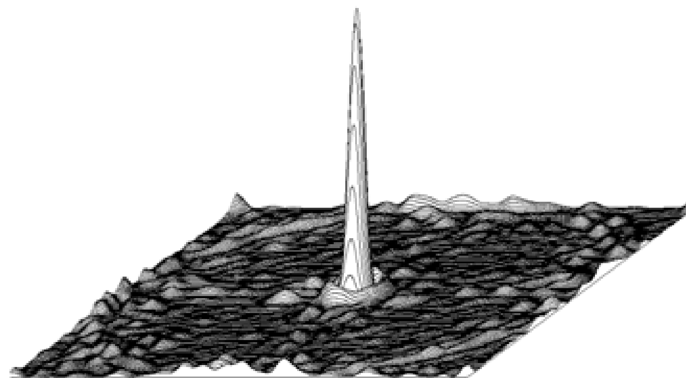

Fig. 2.7. Huygens point spread function by micromirror array lens

diameter of the lens. The schematic of optical simulation is shown in Fig. 2.6. The magnification of the simulated imaging system is 1.0 and a wavelength of 632.8nm was used. A reflectivity of 100% was used for the micromirror's surface. The image distance is 50mm and the lens diameter is 1.8mm, resulting in a NA of 0.018.

The point spread function (PSF) of an imaging system using the MMAL is shown in Fig. 2.7. The resolution of the MMAL is approximately 22μm, whereas the resolution of a perfect aberration-free lens is 21.4μm for the NA of 0.018. Thus, the resolution of the MMAL is essentially the same as a perfect lens. The simulated Strehl ratio, which is the ratio of the PSF maximum intensity to the maximum intensity for a theoretical diffraction-limited PSF is 31.2%.

CHAPTER III

ELECTRO-MECHANICAL DESIGN

3.1 Overview of static characteristics of phase modulation micromirror

A schematic view of a phase modulation micromirror driven electrostatically is shown in Fig. 3.1. If a plate is pulled quasi-statically by electrostatic force, the static displacement of the plate is determined at the point where the electrostatic force and the restoring force by spring are in equilibrium. But as the plate moves to the other plate continuously, the electrostatic force becomes to be larger than the restoring force and the plate is pulled down abruptly. A voltage at this point is pull-in voltage. In case of phase modulation micromirror, the electrostatic force, F_e, between two plates and the restoring force, F_r, are given as follows:

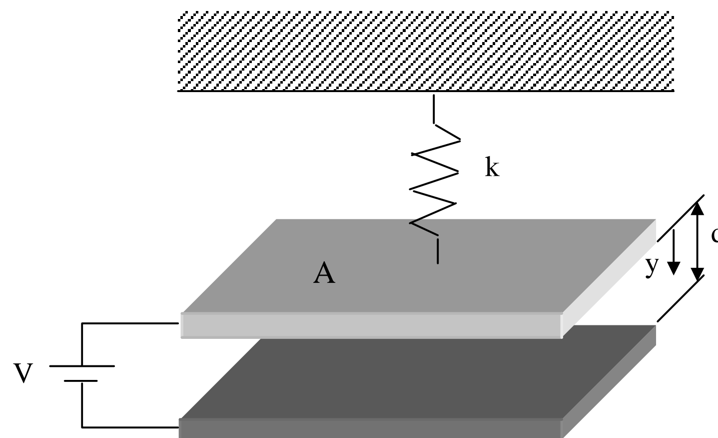

Fig. 3.1. Schematic view of an electrostatically driven phase modulation micromirror

$$F_e = \frac{1}{2}\frac{\varepsilon A V^2}{(d-y)^2} \tag{3.1}$$

$$F_r = ky \tag{3.2}$$

where ε is the permittivity of the air, A is the surface area of the plate, d is the initial distance, k is the stiffness of the spring, y is the displacement, and V is an applied voltage. The displacement y at different voltages is obtained from the demand for the balance of the electrical and mechanical forces, i.e. , $F_e = F_r$.

$$y^3 - 2dy^2 + d^2 y - \frac{\varepsilon A V^2}{2k} = 0 \tag{3.3}$$

Eq(3.4) is used in the inverse form, which is easier to solve:

$$V = \sqrt{\frac{2ky(d-y)^2}{\varepsilon A}} \tag{3.4}$$

At the displacement y = d/3 = y_{pull_in} , the function V(y) reaches its maximum value, V_{pull_in} by solving dV/dy = 0 :

$$V\left(y_{pull_in}\right) = V_{pull_in} = \sqrt{\frac{8kd^3}{27\varepsilon A}} \tag{3.5}$$

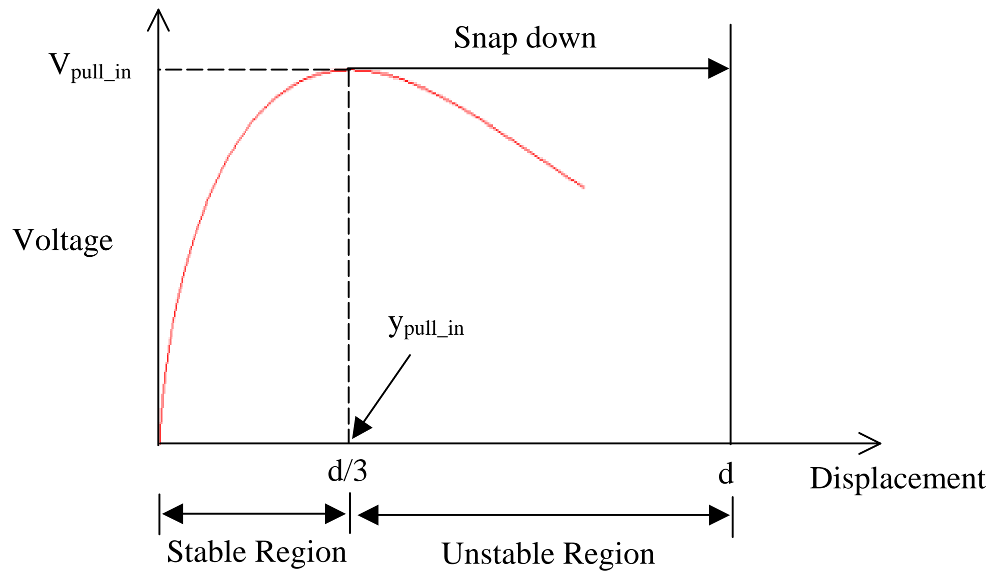

Fig. 3.2. Displacement behavior of the upper plate of a capacitor

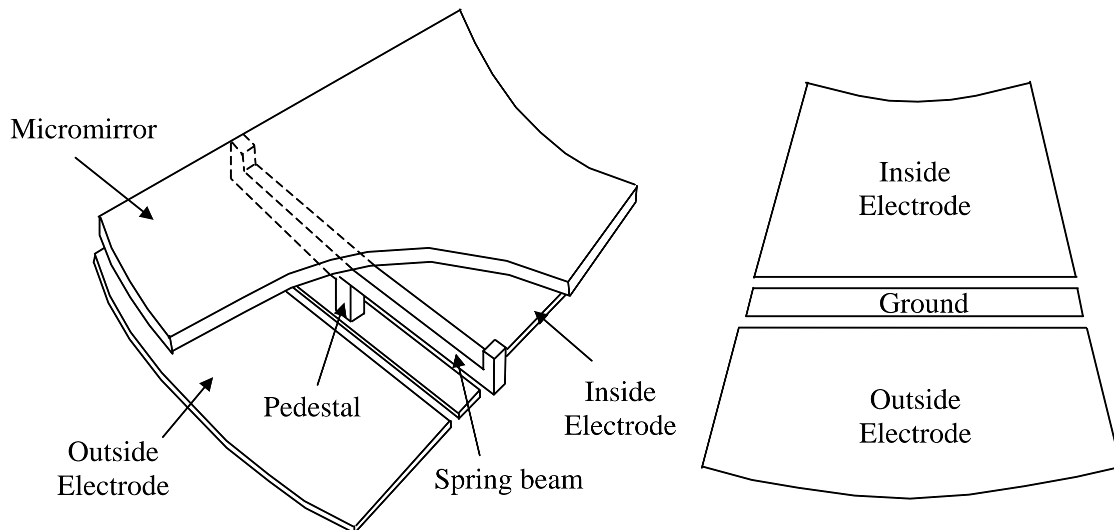

Fig. 3.3. Schematic 3-D view of the micromirror and electrode shape

For voltages V < V_{pull_in} (i.e., displacement $y < y_{pull_in}$), the upper plate resides in a stable region. For V > V_{pull_in} (i.e., displacement $y > y_{pull_in}$), the upper plate collapses towards the counter electrode. This bistable characteristic of the plate capacitor model is shown in Fig. 3.2.

3.2 Structure of the micromirror of MMAL

A three-dimensional view of the micromirror of MMAL with suspension spring, pedestal, and electrodes is shown in Fig. 3.3. For each mirror, the three electrodes are held at separate potentials to control both translational and rotational motion. Every mirror at a given radius is controlled by one pair of circular electrodes and a circular ground electrode (Fig. 3.4).

Suspension spring has two kinds of deformation, bending and torsion at the same time. The torsion of suspension spring causes a rotational motion of the micromirror and the bending of

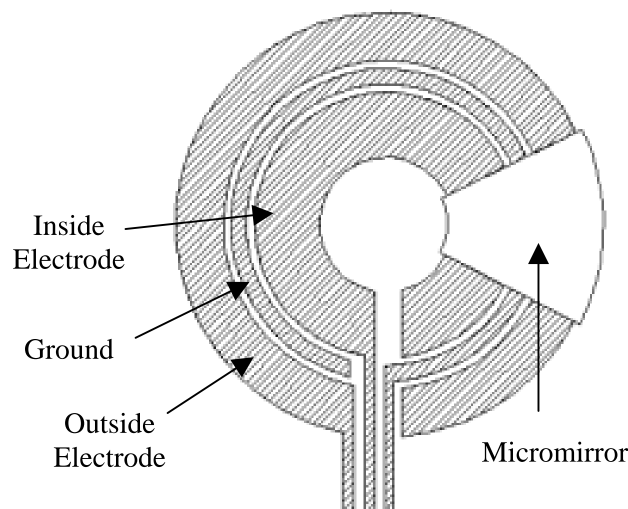

Fig. 3.4. Electrode pair of circular shape

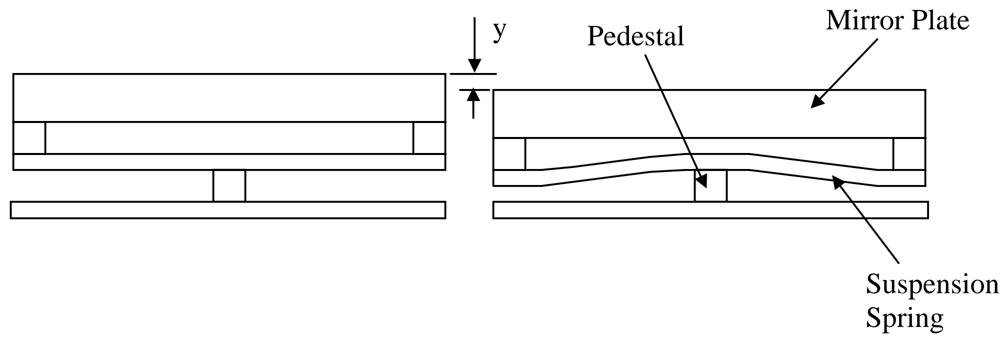

Fig. 3.5. Translation by bending of a suspension spring

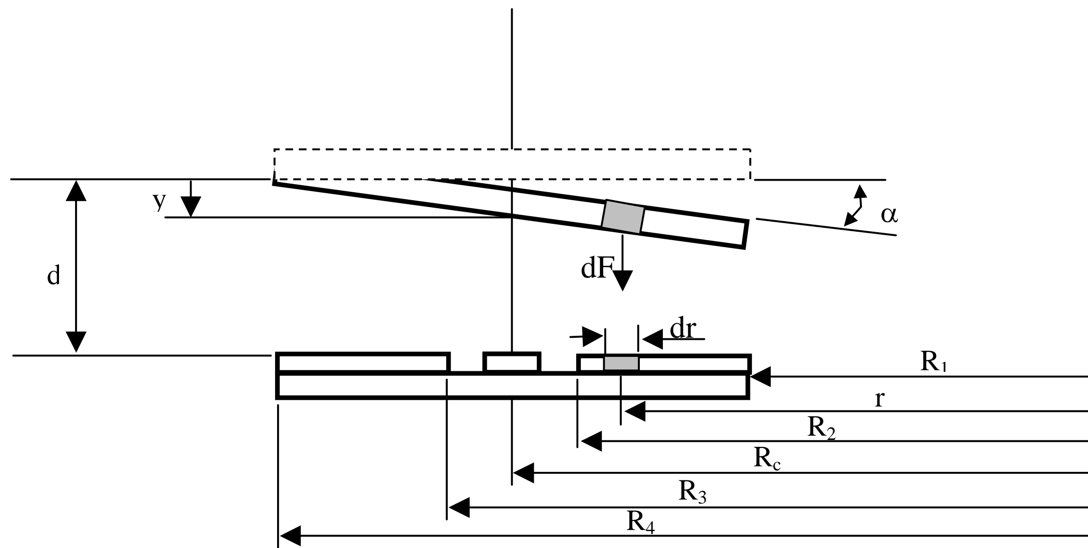

Fig. 3.6. Cross-sectional view of the micromirror

suspension spring causes a translational motion as shown in Fig. 3.5. Since the suspension spring is much more flexible than the pedestal and the mirror plate, it has zero slope at each ends, which are fixed to the pedestal and the mirror plate.

3.3 Electrostatic force and torque

The micromirror can be driven to translate and rotate by adding voltage between the micromirror and two electrodes. When the micromirror has rotational displacement, a force and torque applied to the micromirror can be calculated by regarding the plate as being composed of an infinite number of infinitesimally small capacitors of width dr (Fig. 3.6). Therefore, the electrostatic forces by inside electrode and outside electrode, F_{ei} and F_{eo} and the electrostatic torque by inside electrode and outside electrode, M_{ei} and M_{eo} are given by

$$\begin{aligned} F_{ei} &= \int_{R_1}^{R_2} dF = \int_{R_1}^{R_2} \frac{1}{2} \frac{V_i^2 \varepsilon}{(d - y - \alpha(R_c - r))^2} dA \\ &= \theta \int_{R_1}^{R_2} \frac{1}{2} \frac{V_i^2 \varepsilon \ r}{(d - y - \alpha(R_c - r))^2} dr \end{aligned} \tag{3.6}$$

$$\begin{aligned} F_{eo} &= \int_{R_3}^{R_4} dF = \int_{R_3}^{R_4} \frac{1}{2} \frac{V_o^2 \varepsilon}{(d - y - \alpha(R_c - r))^2} dA \\ &= \theta \int_{R_3}^{R_4} \frac{1}{2} \frac{V_o^2 \varepsilon \ r}{(d - y - \alpha(R_c - r))^2} dr \end{aligned} \tag{3.7}$$

$$M_{ei} = \int_{R_1}^{R_2} (R_c - r) dF = \theta \int_{R_1}^{R_2} \frac{1}{2} \frac{\left(R_c - r\right) \ V_i^2 \varepsilon \ r}{\left(d - y - \alpha\left(R_c - r\right)\right)^2} dr \tag{3.8}$$

$$M_{eo} = \int_{R_3}^{R_4} (R_c - r) dF = \theta \int_{R_3}^{R_4} \frac{1}{2} \frac{\left(R_c - r\right) \ V_o^2 \varepsilon \ r}{\left(d - y - \alpha\left(R_c - r\right)\right)^2} dr \tag{3.9}$$

where, V_i is a voltage of inside electrode, V_o is a voltage of outside electrode, and ε is the permittivity of air (ε=8.85pF/m). In Fig. 3.6, R_c, R_1, R_2, R_3 and R_4 are radial position of suspension spring, inside electrode, and outside electrode from the center of MMAL. θ is an angle of a mirror plate with fan shape and d is an initial gap between a micromirror plate and electrode at zero voltage. r and dr represents the radial position and the width of the infinitesimal capacitor used for integration. y represents translational displacement and α represents rotational displacement. The radial width of micromirror plate is fixed as 100μm. The area of the micromirror plate (around 10000μm^2) has been defined in order to have almost the same voltage range for each radius of mirrors.

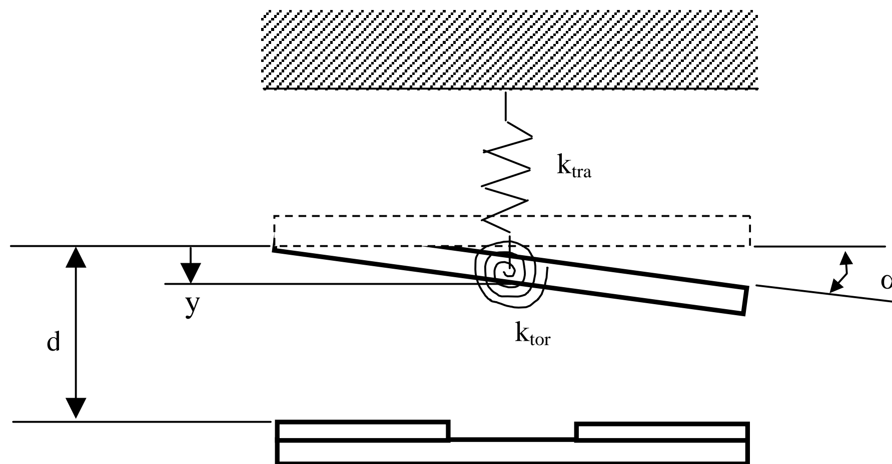

Fig. 3.7. Schematic view of a micromirror with translational and rotational displacement

3.4 Elastic recovery force and torque

Fig. 3.7 is a schematic view of a micromirror with translational and rotational displacement. Since the elastic recovery force and torque of the micromirror are determined by translational stiffness (k_{tra}) and torsional stiffness (k_{tor}) at a given displacement, they need to be calculated. Translational and torsional stiffness are given at Eq. (3.10) and Eq. (3.11), which are determined by assuming that both ends of beam are clamped:

$$k_{tra} = 2\times\frac{12EI}{L^3} = \frac{2Ebh^3}{L^3} \tag{3.10}$$

$$k_{tor} = 2\times\frac{cGbh^3}{L} = \frac{2cGbh^3}{L} \tag{3.11}$$

Table. 3.1. Mechanical properties and dimensions of a spring for a micromirror furthest from the lens center

Dimensions	b	3.5μm
	h	2μm
	L	46μm
Mechanical properties (polysilicon)	E	170GPa
	G	66GPa
Coefficient for torsion of rectangular shaft	c	0.218

where, E is Young's modulus, G is the shear modulus, I is the moment of inertia, b is the spring width, h is the spring thickness, L is the length of spring, and c is a constant that depends on the ratio of spring width and spring thickness. The mechanical properties of polysilicon [38] and the dimensions of the mirrors furthest from the lens center are given in Table 3.1, which give a translational stiffness of 97.8N/m and a torsional stiffness of 1.75×10^{-8} N·m.

The elastic recovery force F_r by the bending of suspension spring and elastic recovery torque M_r by the torsion of the suspension spring can be expressed as

$$F_r = k_{tra} \cdot y = \frac{2Ebh^3 y}{L^3} \tag{3.12}$$

$$M_r = k_{tor} \cdot \alpha = \frac{2cGbh^3 \alpha}{L} \alpha \tag{3.13}$$

3.5 Static behavior

When the micromirror is driven to translate and rotate by electrostatic force and torque, the translational and rotational displacement of a suspension spring will generate an elastic recovery force and torque. Therefore, the micromirror becomes steady only when these force and torque are balanced (i.e. at the static equilibrium condition) and the static behavior of the micromirror is determined by two static equations, force equation (Eq. (3.14)) and moment equation(Eq. (3.15)), with two variables, translational displacement (y) and rotational displacement (α).

$$\mathrm{F_r} = \mathrm{F_{ei}} + \mathrm{F_{eo}} \tag{3.14}$$

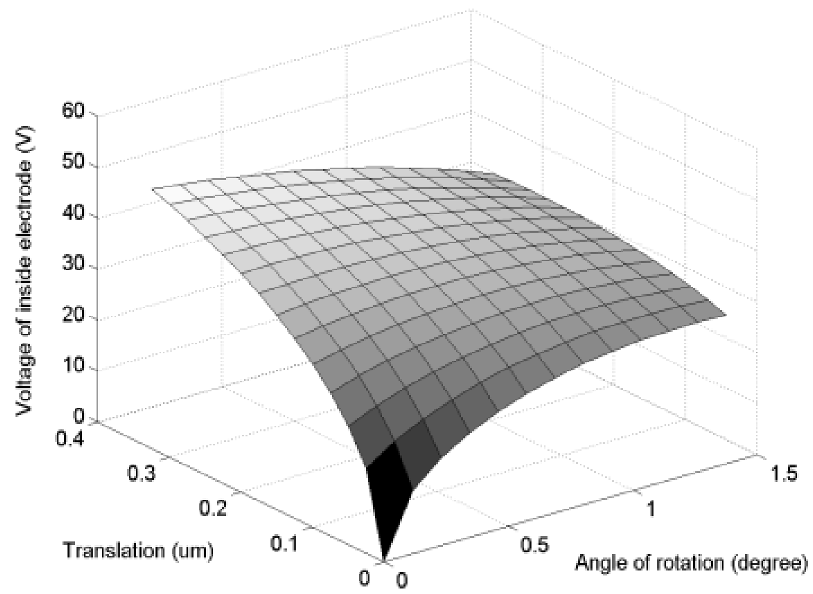

Fig. 3.8. Simulated plot of inside voltage versus translation and rotation

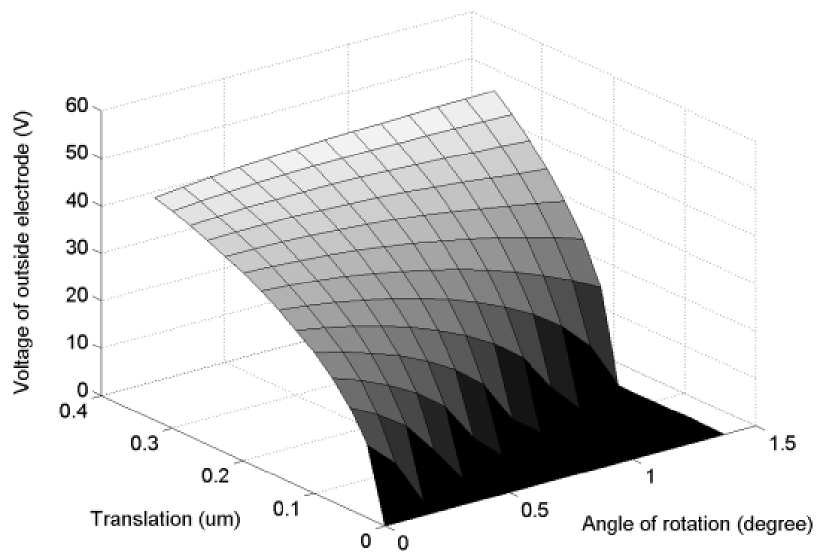

Fig. 3.9. Simulated plot of outside voltage versus translation and rotation

$$M_r = M_{ei} + M_{eo} \tag{3.15}$$

Fig. 3.8 is a simulated plot of the inside electrode voltage versus translation and rotation. Fig. 3.9 is a simulated plot of outside electrode voltage versus translation and rotation. Fig. 3.8 and Fig. 3.9 are determined by finding an inside electrode voltage, V_i and an outside electrode voltage, V_o from Eq. (3.14) and Eq. (3.15) when a desired translational and rotational amount are given.

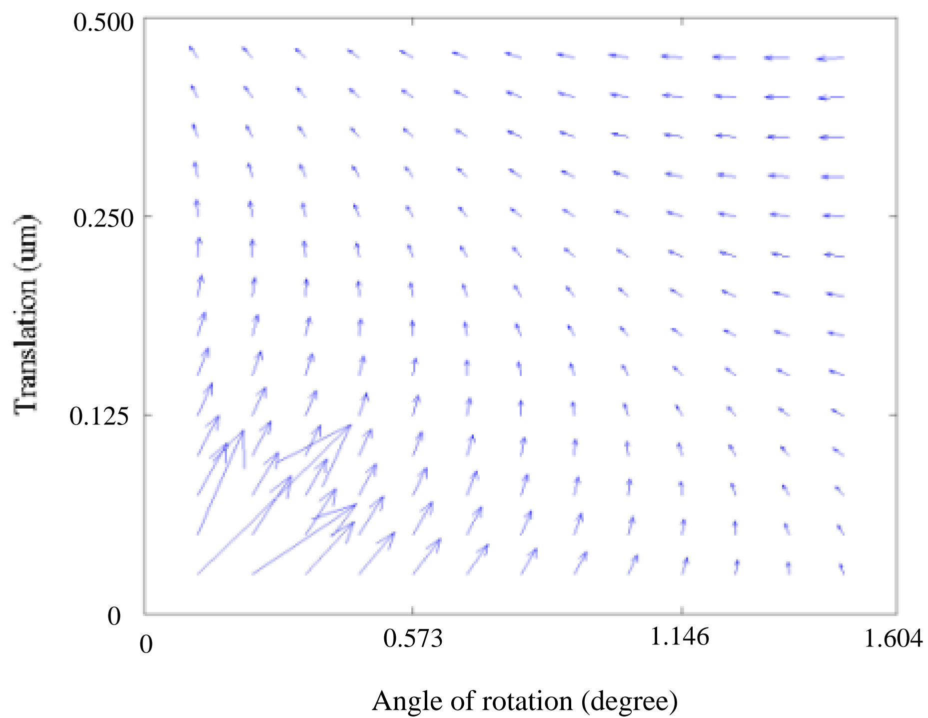

Fig. 3.10. Simulated plot of the gradient of inside voltage versus translation and rotation

3.6 Stability

Electrostatic actuators undergo the classical pull-in instability when the electric force exceeds the elastic force (for recent developments see [39] and [40]). Since the pull-in point determines

the translational and rotational range, it is an important parameter. The maximum driving voltage V_{max} is also another important parameter in considering practical usage. To be compatible with IC components, which normally operated at 5V, and to prevent electrical breakdown, the maximum value of the driving voltage should generally be as low as possible.

Theoretically, the pull-in point can be obtained by finding $dV/dx = 0$. For pure translation, there is no instability for a translation less than 666nm, 1/3 of the gap between the electrode and mirror. However, the mirror having two coupled degrees of freedom has a different instability point. Fig. 3.10 is a plot of voltage gradient of Fig. 3.8. The inside voltage is always larger than the outside voltage because a positive angle of rotation is only possible by the larger inside voltage. Therefore, the instability point can always be determined by the inside voltage. The mirror becomes unstable when either component of the gradient in Fig. 3.10 is negative, i.e. when the partial derivative of the inside electrode voltage with respect to either the translation or the rotation is negative. As Fig. 3.10 illustrates, the translational range is less than 316nm, the requirement for λ=632nm at an arbitrary angle of rotation, because a rotational pull-in instability occurs before reaching a translation of 316nm. It is shown that a negative gradient in the rotational direction exists in Fig. 3.10.

The designed micromirror does not have enough translation to make the proposed MMAL. In this research, it is necessary to estimate a feasible imaging performance in case that the proposed MMAL has a sufficient translation. Therefore, the focal length of MMAL with relatively small translation will be found to minimize the aberration by insufficient translation in CHAPTER VI.

CHAPTER IV

FABRICATION

4.1 MUMPs technology

Until recently, research into microelectromechanical systems(MEMS) was restricted to institutions that had access to private fabrication facilities that could meet the specialized demands of micromachining. However, the growing number of commercial micromachining foundries is making the technology widely available. The low cost and frequently scheduled fabrication runs of commercial foundry processes reduce the scheduling and financial risk of prototyping useful MEMS solutions.

Table. 4.1. Structural and sacrificial layers used in MUMPs

Layer name	Nominal thickness (μm)
Nitride (silicon nitride)	0.60
Poly-0 (bottom polysilicon layer)	0.50
1st Oxide (sacrificial layer - phosphosilicate glass)	2.0
Poly-1 (middle polysilicon layer)	2.0
2nd Oxide (sacrificial layer - phosphosilicate glass)	0.75
Poly-2 (top polysilicon layer)	1.50
Metal (gold)	0.50

A disadvantage of this approach is that the users of a foundry service have little control over important design parameters such as layer thickness and choice of materials, so their designs are constrained by more than just the mask layout design rules. Even though a foundry service has little control over design parameters, it is appropriate for prototyping the micromirror array lens.

One of popular commercial surface micromachining processes for MEMS is the Multi-User MEMS Processes(MUMPs®), which is performed by Cronos. Design rules, fabrication details, and example devices are available on the World Wide Web sites (http://www. memsrus.com/CIMSsvcs .html) maintained by Cronos.

MUMPs® is a three-layer polycrystalline silicon (polysilicon) process. It is intended for prototyping MEMS, using surface-micromachined thin films on a silicon wafer. MUMPs® offers three patternable layers of polysilicon and two sacrificial layers of phosphosilicate glass on a base layer of silicon nitride. A top layer of gold is provided as the reflective and/or conductive surface. Table. 4.1 identifies the layer thickness for each of the films used in MUMPs®, with deposition order of the films on the silicon wafer

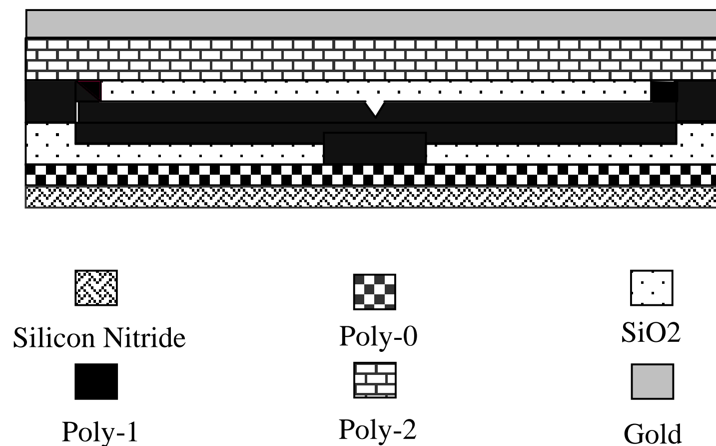

Fig. 4.1. Cross-sectional view of the micromirror fabricated by MUMPs

substrate, with silicon nitride being the first layer and Fig. 4.1 illustrates the MUMPs® layers. The order of the entries in Table. 4.1 is consistent with the deposition order of the films on the silicon wafer substrate. MUMPs® surface micromachining process consists of the following layers: silicon nitride (0.6μm), the first polysilicon layer (Poly-0, 0.5μm), the first phosphosilicate glass layer (2.0μm), the second polysilicon layer (Poly-1, 2.0μm), the second phosphosilicate glass layer (0.75μm), the third polysilicon layer (Poly-2, 1.5μm), and a metal (gold) layer (0.5μm). Each polysilicon layer is doped with phosphorous to make the polysilicon a conductor. Gold is evaporated onto the device after all other layers have been deposited by low pressure chemical vapor deposition (LPCVD). The polysilicon layer and <100>-cut silicon substrate are highly doped with phosphorus to decrease electrical resistance. After construction, the micromachined device is release by removing the sacrificial glass layers in a bath of buffered hydrofluoric acid.

After the devices are released, residual material stresses in the gold layer (tensile) and Poly-2 layer (compressive) may cause the reflective surface to curl slightly into a concave shape [41]. Typical peak-to-valley curvature for a 100μm wide gold on a Poly-2 micromirror was measured as 495nm [41]. Combining the top and middle polysilicon layers (stacked poly) as support for the gold layer reduced peak-to-valley curvature of a 100 μm wide micromirror to 140nm [41]. Peak-to-valley curvature was further reduced to 63nm by retaining the second oxide layer between the top and middle polysilicon layers (trapped oxide) [41].

In surface micromachining, the thin-film layers conform closely to the topology of the previously deposited and patterned layers (Fig. 4.1). Unless the designer makes sure a layer is flat by controlling the pattern of the layers beneath it, the induced topology can have detrimental effects on the layer's flatness and the effective elastic modulus of mechanical structures. In

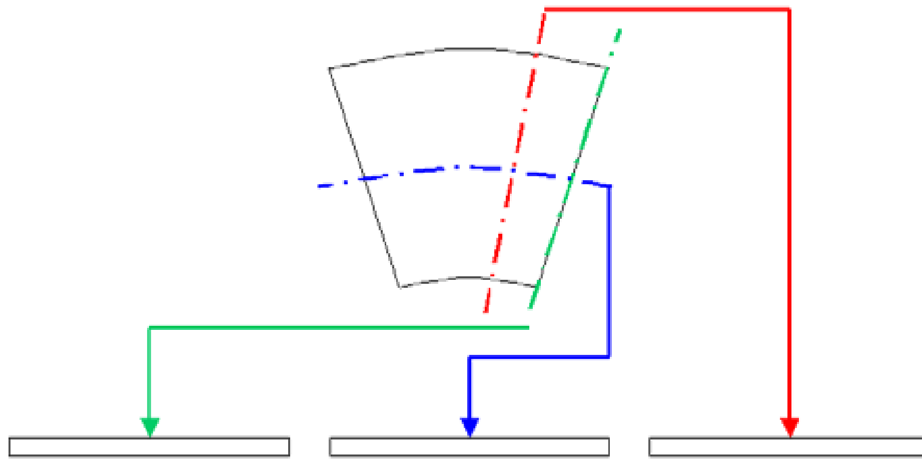

Fig. 4.2. Three different cross sectional views of the micromirror

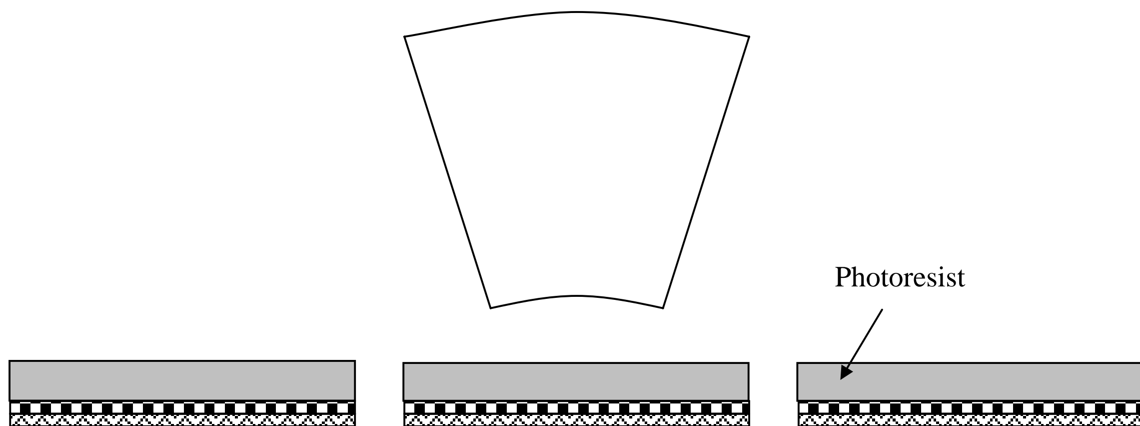

Fig. 4.3. The UV-sensitive photoresist

extreme cases, the topology can trap part of a structure that was intended to move freely. This problem of surface topology can be controlled in more sophisticated surface micromachining processes, where layers are chemically mechanically polished prior to subsequent layer deposition [42].

4.2 Micromirror fabrication using MUMPs

Three different cross sectional views of the device are used to make it easier to understand as shown in Fig. 4.2. First of all, a 0.6μm LPCVD (low pressure chemical vapor deposition) silicon nitride layer is deposited on the wafers as an electrical isolation layer. This is followed directly by the deposition of a 0.5μm LPCVD polysilicon film-Poly 0. Poly 0 is then patterned by photolithography, a process that includes the coating of the wafers with photoresist (Fig. 4.3), exposure of the photoresist with the appropriate mask and developing the exposed photoresist to

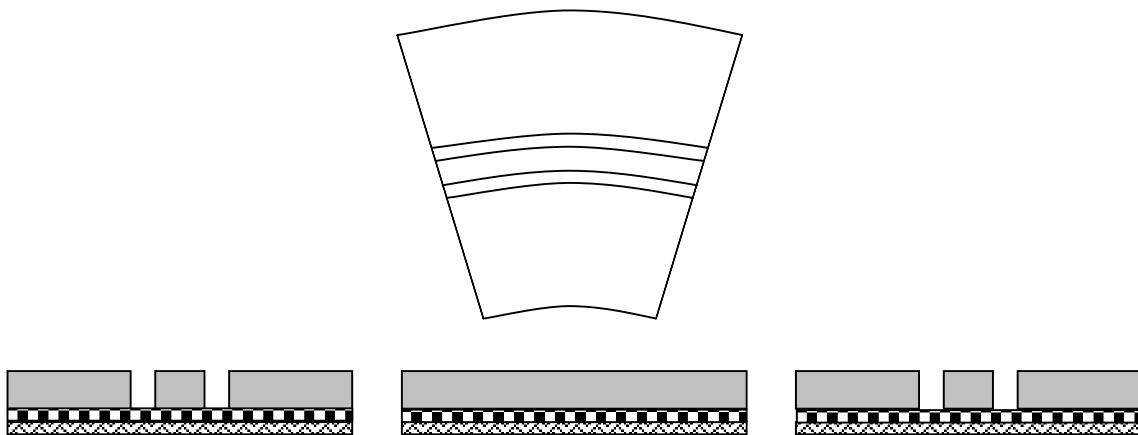

Fig. 4.4. The lithographically patterned photoresist to remove unwanted Poly 0 layer

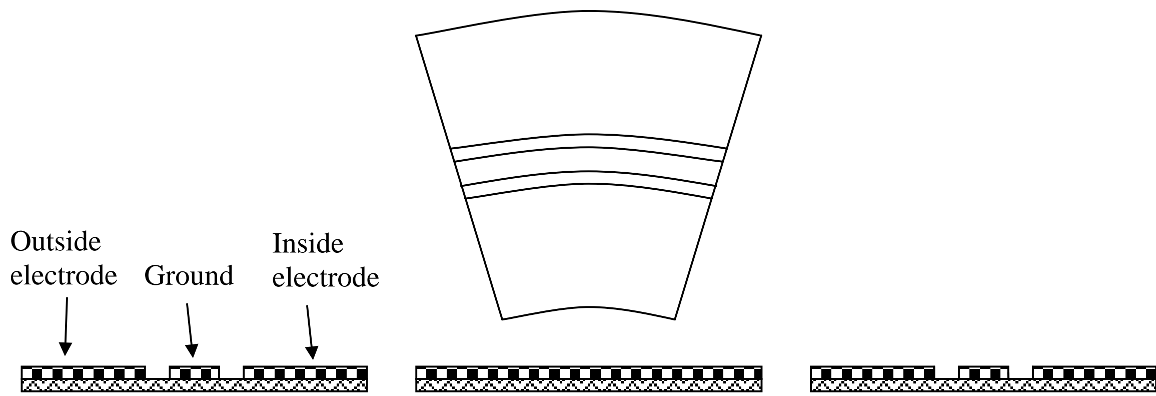

Fig. 4.5. The Poly 0 layer patterned by reactive ion etching (RIE)

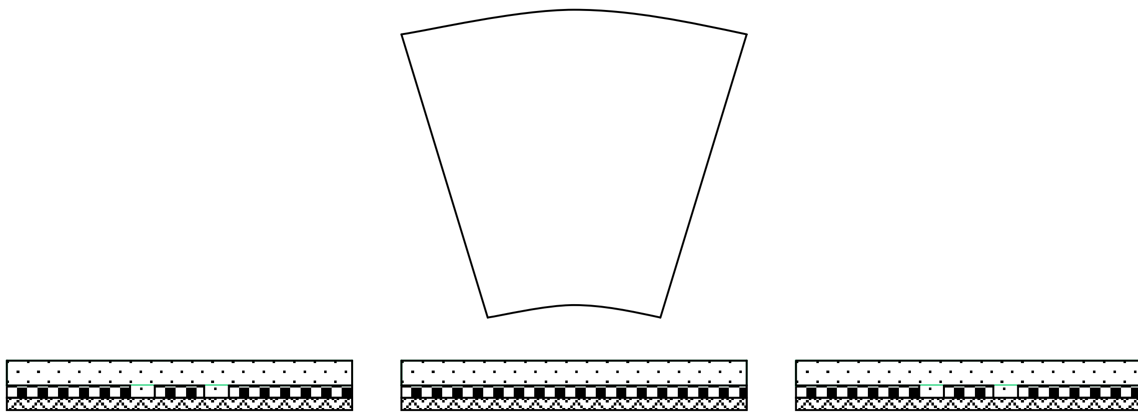

Fig. 4.6. A 2.0μm layer of PSG by low pressure chemical vapor deposition (LPCVD)

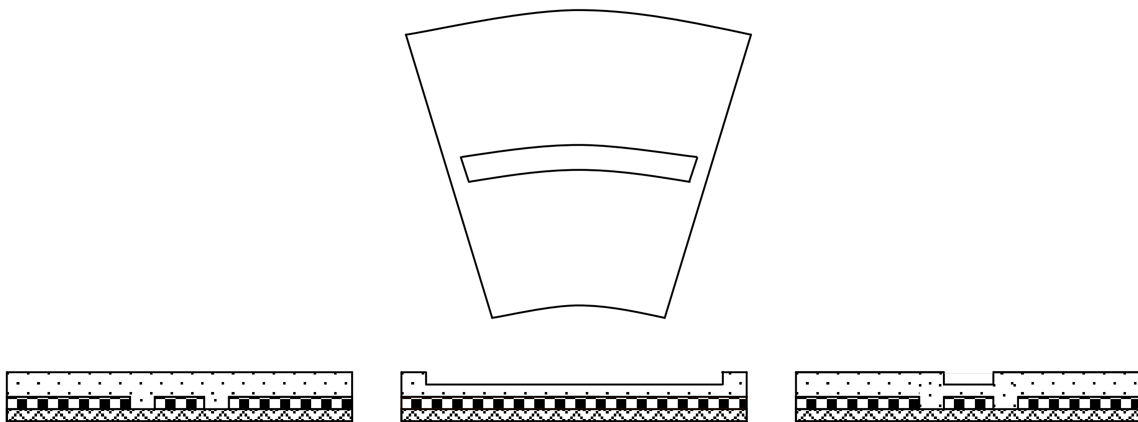

Fig. 4.7. The dimples with 750nm deep by RIE

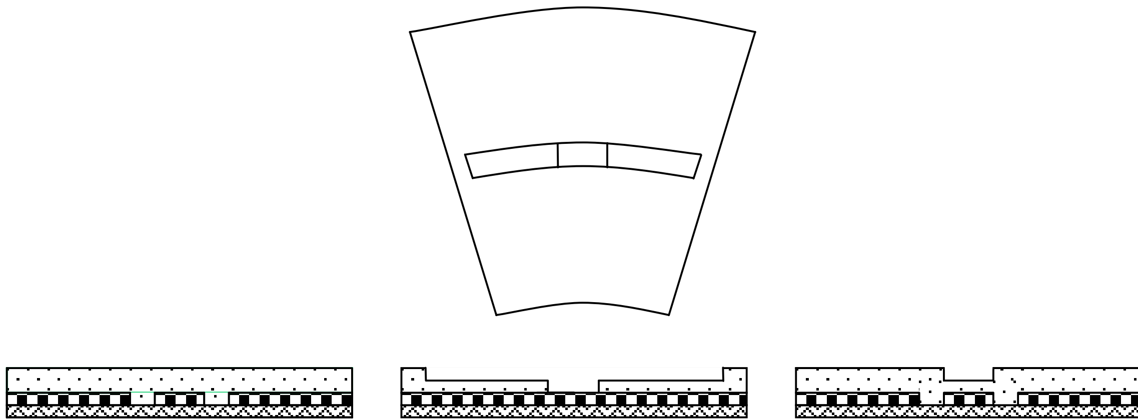

Fig. 4.8. The oxide layer patterned by RIE

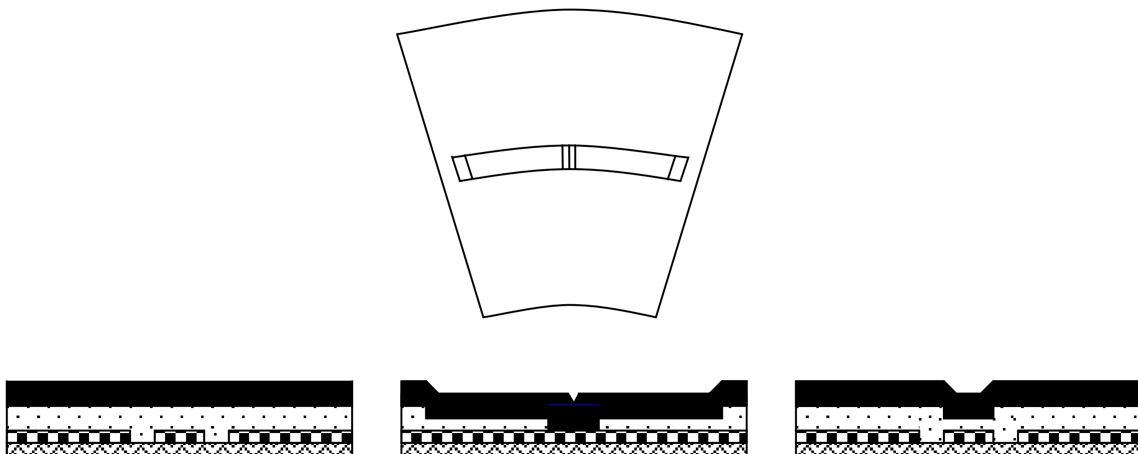

Fig. 4.9. A blanket 2.0μm layer of Poly 1 deposited by LPCVD

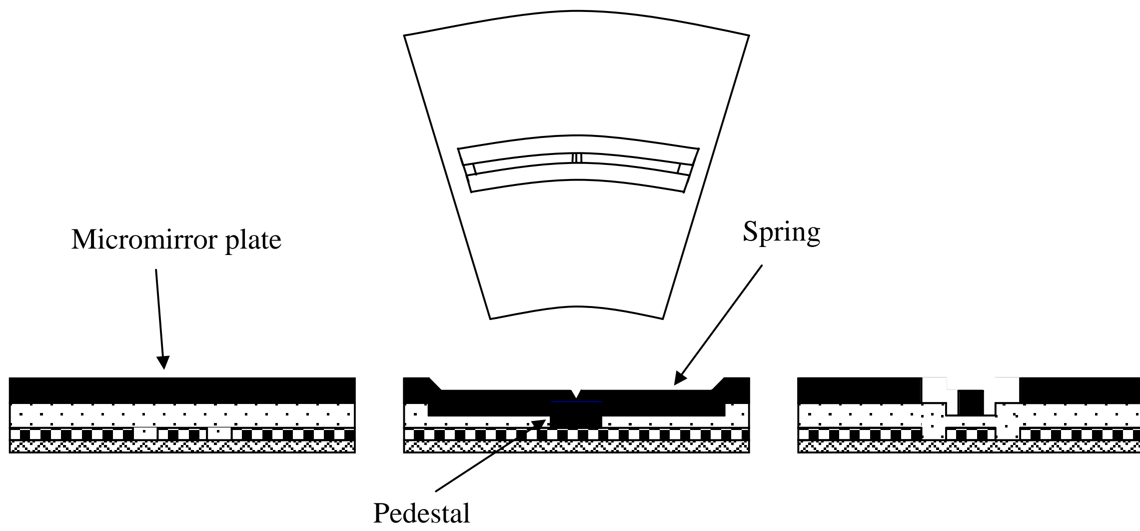

Fig. 4.10. Poly 1 layer patterned by RIE

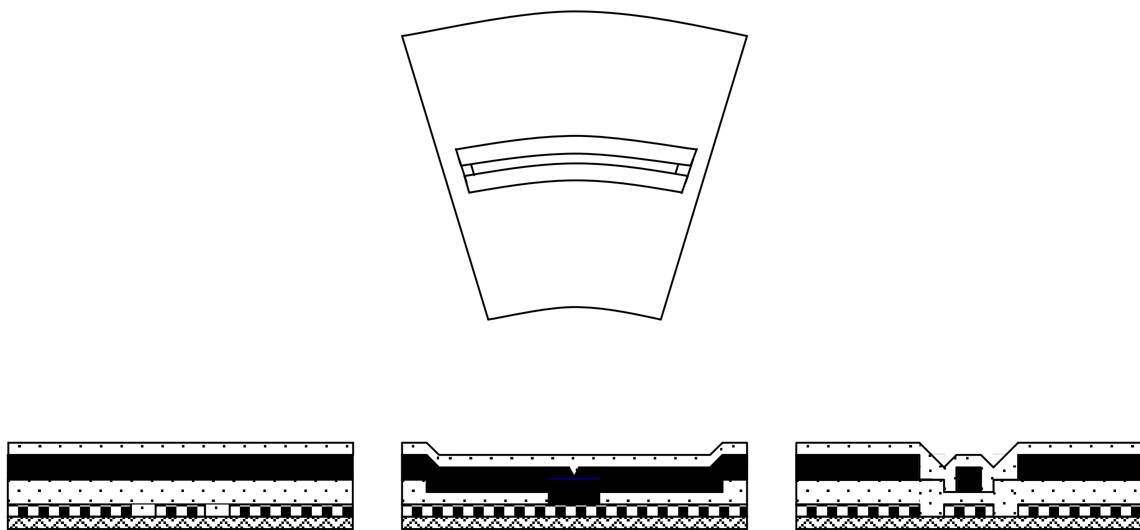

Fig. 4.11. The second oxide layer, 0.75μm of PSG

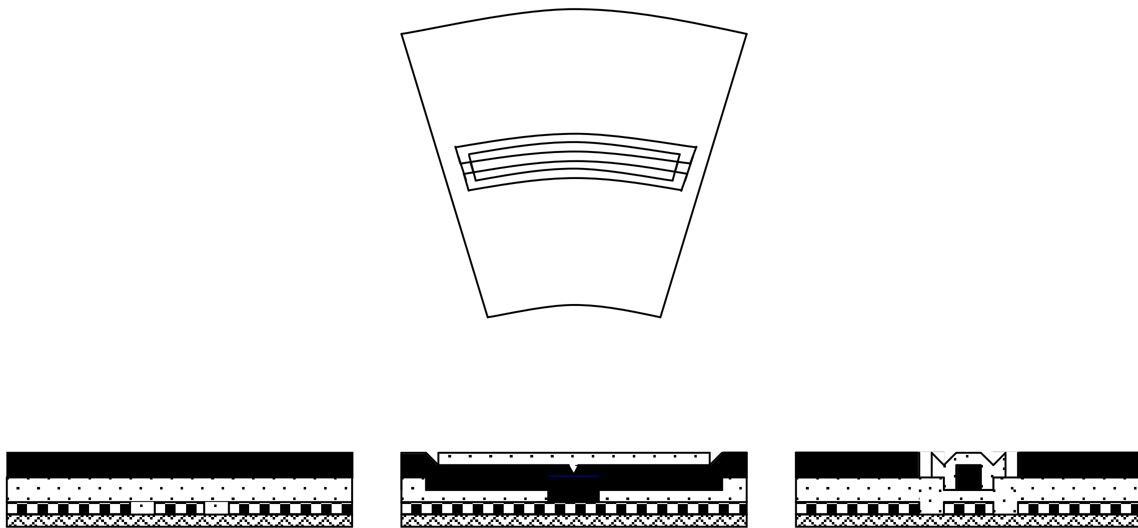

Fig. 4.12. The second oxide layer patterned by RIE

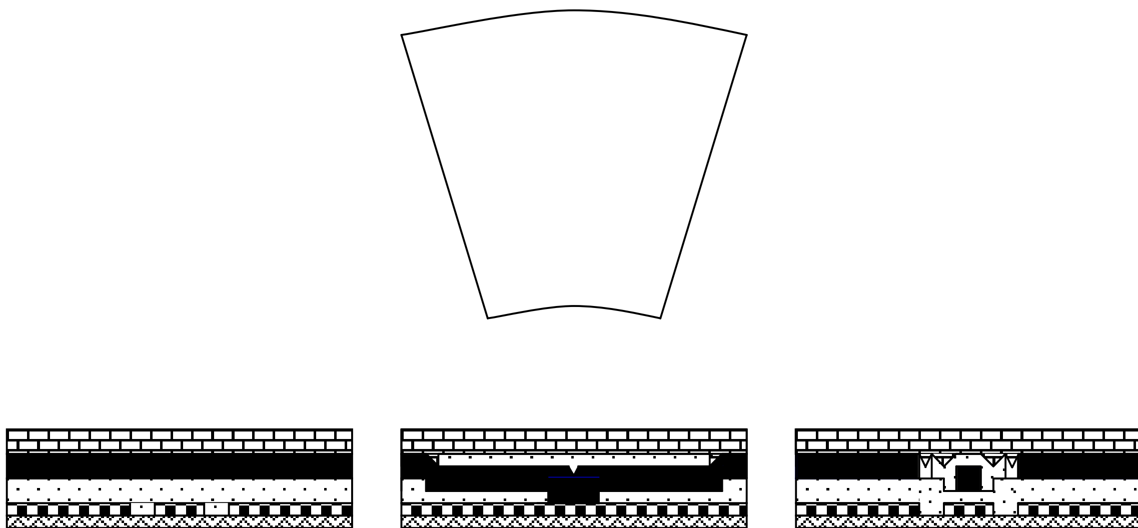

Fig. 4.13. A blanket 1.5μm layer of Poly 2 deposited by LPCVD

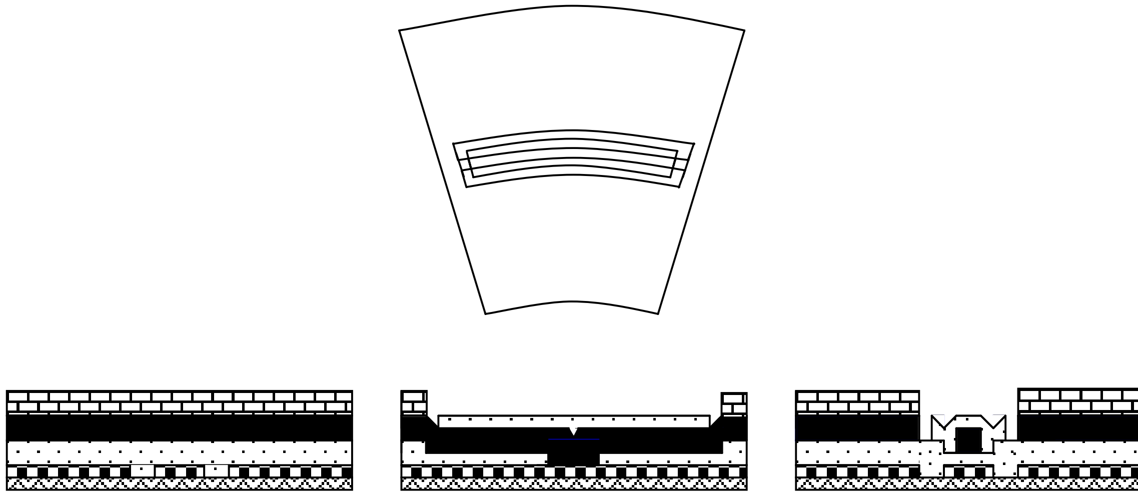

Fig. 4.14. Poly 2 layer patterned by RIE

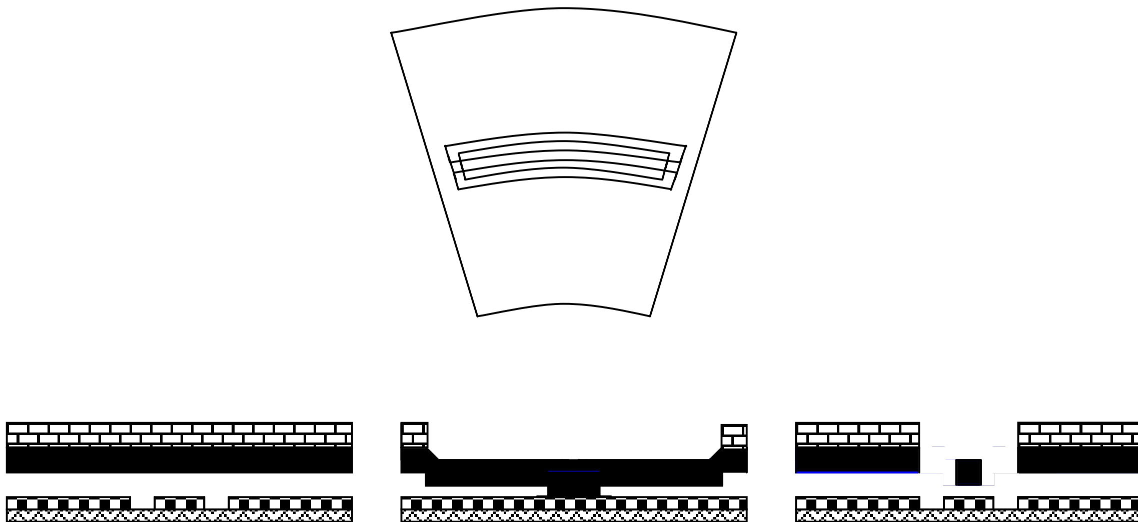

Fig. 4.15. The micromirror released by immersing the chips in a 48% HF solution

create an etch mask for the bottom electrode of a micromirror (Fig. 4.4). After patterning the photoresist, the Poly 0 layer is then etched in an RIE (Reactive Ion Etch) system (Fig. 4.5). A 2.0μm phosphosilicate glass (PSG) sacrificial layer is then deposited by LPCVD (Fig. 4.6) and then annealed . This layer of PSG, known as First Oxide, is removed at the end of the process to free the first mechanical layer of polysilicon (pedestal, spring and micromirror plate). The sacrificial layer is lithographically patterned with the DIMPLES mask and the dimples are transferred into the sacrificial PSG layer by RIE, as shown in Fig. 4.7. The nominal depth of the dimples is 0.75μm. The wafers are then patterned with the third mask layer, ANCHOR1, and reactive ion etched (Fig. 4.8). This step provides anchor holes that will be filled by Poly 1. They provide a mechanical and electrical connection between the ground of bottom electrode(Poly 0) and the pedestal, spring and micromirror plate(Poly 1). After etching ANCHOR1, the first structural layer of polysilicon (Poly 1) is deposited at a thickness of 2.0μm (Fig. 4.9). A thin (0.2μm) layer of PSG is deposited over the polysilicon and the wafer is annealed at both above and below it. The anneal also serves to significantly reduce the net stress in Poly 1 to form the pedestal, spring and micromirror plate. The PSG layer is etched to produce a hard mask for the subsequent polysilicon etch. The hard mask is more resistant to the polysilicon etch chemistry than the photoresist and ensures better transfer of the pattern into the polysilicon. After etching the polysilicon (Fig. 4.10), the photoresist is stripped and the remaining oxide hard mask is removed by RIE. After Poly 1 is etched, a second PSG layer (Second Oxide) is deposited and annealed (Fig. 4.11). The Second Oxide is patterned using two different etch masks with different objectives. The POLY1_POLY2_VIA also provides a mechanical and electrical connection between the Poly 1 and Poly 2 layers. The POLY1_POLY2_VIA layer is

lithographically patterned and etched by RIE (Fig. 4.12). The ANCHOR2 level is usually provided to etch both the First and Second Oxide layers in one step, thereby eliminating any misalignment between separately etched holes. But, ANCHOR2 level is not used because the micromirror doesn't have etched holes to increase total reflective surface area of a micromirror. The second structural layer, Poly 2, is then deposited (1.5μm thick) followed by the deposition of 0.2μm PSG (Fig. 4.13). Area of the Poly 2 layer above a spring structure is etched because the topology induced by complicate the spring and the bottom electrode pattern can cause detrimental effects to the layer's flatness. The photoresist then is stripped and the masking oxide is removed (Fig. 4.14). The final layer in the MUMPs process is a 0.5μm metal layer. But the metal layer causes a deformation of micromirror by thermal residual stress. Therefore, the deposited metal is removed thoroughly using lift-off. Finally, the wafer is diced, and shipped for sacrificial release. The final step is to release a structure by removing Oxide 1 and Oxide 2. The final, released structure is shown in Fig. 4.15.

4.3 Post processing

The releasing process was conducted in the cleanroom of the TAMU Materials Characterization Facility (MCF). Unreleased dies were delivered from Cronos with a protective photoresist layer on top, which was removed in a 30 minute acetone bath. The die was then rinsed in isopropyl alcohol for 10 minutes and rinsed in deionized water for 10 minutes.

Most of released MMALs did not work because the micromirrors and electrodes were shorted at some radii. The short was caused by conductive particles. Even if only one conductive particle stays between the micromirror and electrode, all micromirrors at that radius are not actuated. Possible sources of conductive particles are the Gold layer and the Chromium layer, which helps Gold layer to adhere the Poly 2 layer. Therefore, the Gold layer and the Chromium

layer were completely etched before releasing a structure. At first, Siloxide with an etching rate of 40 Å/sec at 25 °C was used because a concentrated hydrofluoric acid (48%) is extremely dangerous. But, Siloxide attacked polysilicon too much. In result, the surface of the micromirror became rough and some leads of Poly 0 layer were completely etched away as shown in Fig. 4.16. Most critical problem of using Siloxide is the stiction of the micromirror. Adhension of the micromirror to the substrate is one of the main difficulties in MMAL fabrication due to inherent proximity (2μm) between the micromirror and the underlying substrate. This phenomenon is called 'stiction' in the field of microelectromechanical systems (MEMS). The most generic procedure to obtain free-standing surface-micromachined structures is to rinse the etchant used to free the structures with deionized (DI) water and simply dry it through evaporation. A micromirror held up by the flexible suspension spring was pulled down to the substrate during drying DI water by the capillary force induced by the droplet in the gap. Because the adhension

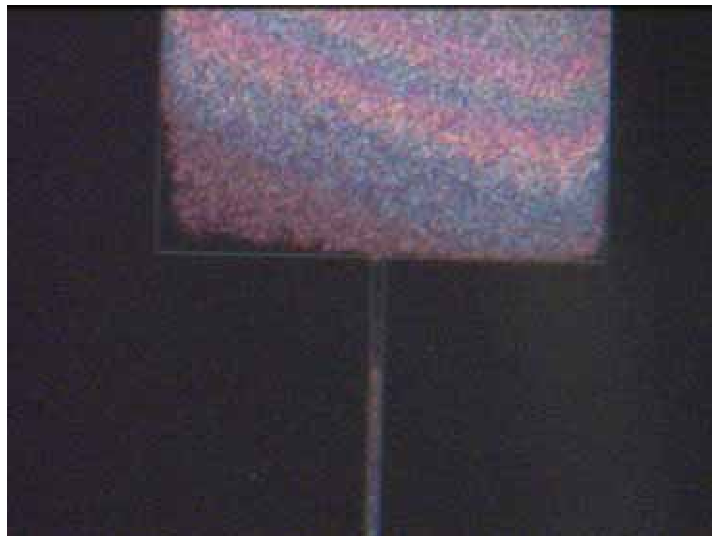

Fig. 4.16. The lead disconnected by Siloxide

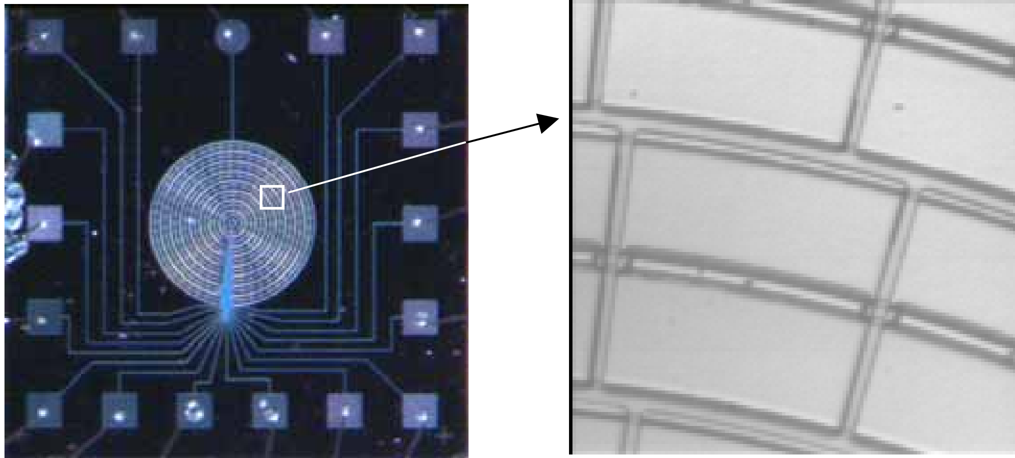

Fig. 4.17. The fabricated micromirror array lens (MMAL)

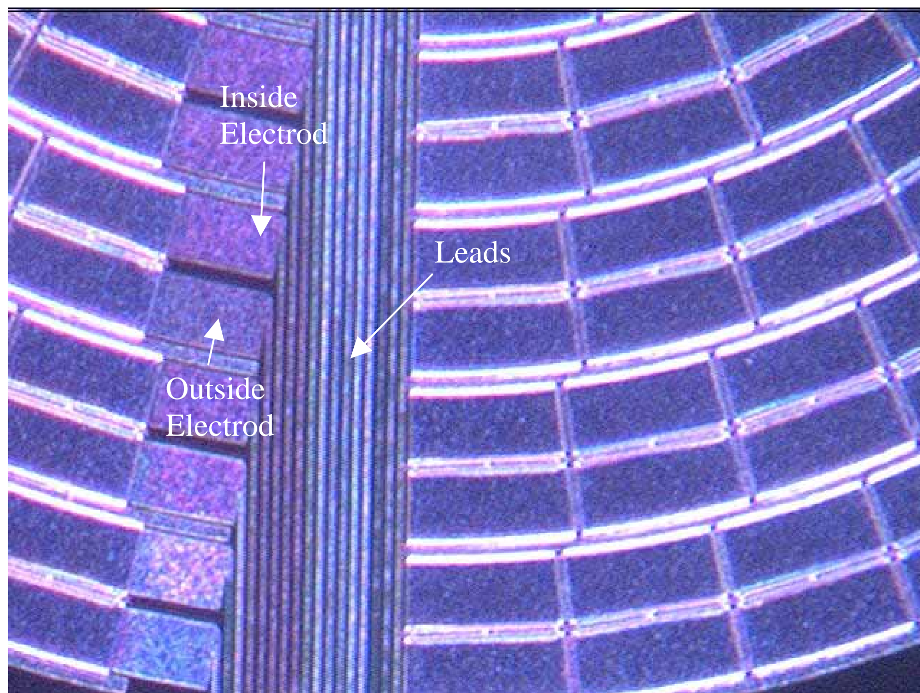

Fig. 4.18. The leads of micromirror array lens

force between the contacted areas is larger than the elastic restoring force of the suspension spring, the micromirror remained stuck to the substrate even after being completely dried. Solid bridging, van der Waals forces, electrostatic forces, and hydrogen bonding make the micromirror to be permanently stuck. The Siloxide made the suspension spring to be thin. Therefore, the stiction of the micromirror occurs by the reduced elastic restoring force.

Concentrated (48%) hydrofluoric acid has a high selectivity, which is more than 100:1. Therefore, the SiO2 sacrificial layers were removed by a 5 minute immersion in concentrated (48%) hydrofluoric acid, which has 10μm/min of an etching rate. The die was immersed in a large volume of continuously flowing DI water for 30 min. Long rinsing in high-quality DI water helps to remove conductive particles between the micromirrors and the electrodes. After the rinse, it was soaked for 15 minutes in isopropyl alcohol, then baked dry in a 110°C oven for 15 minutes. The isopropyl alcohol displaces the water, and when it evaporates, its lower surface tension prevents stiction/pull-down of the mirror [43]. Fig. 4.17 and Fig. 4.18 are the photographs of a released MMAL.

CHAPTER V

EXPERIMENT

5.1 Measurement

Interferometry optical profilers are non-contact instruments for the measurement of microscopic surface height profiles and therefore do not harm the surface under test. They are widely used in precise linear displacement measurement such as semiconductor metrology and

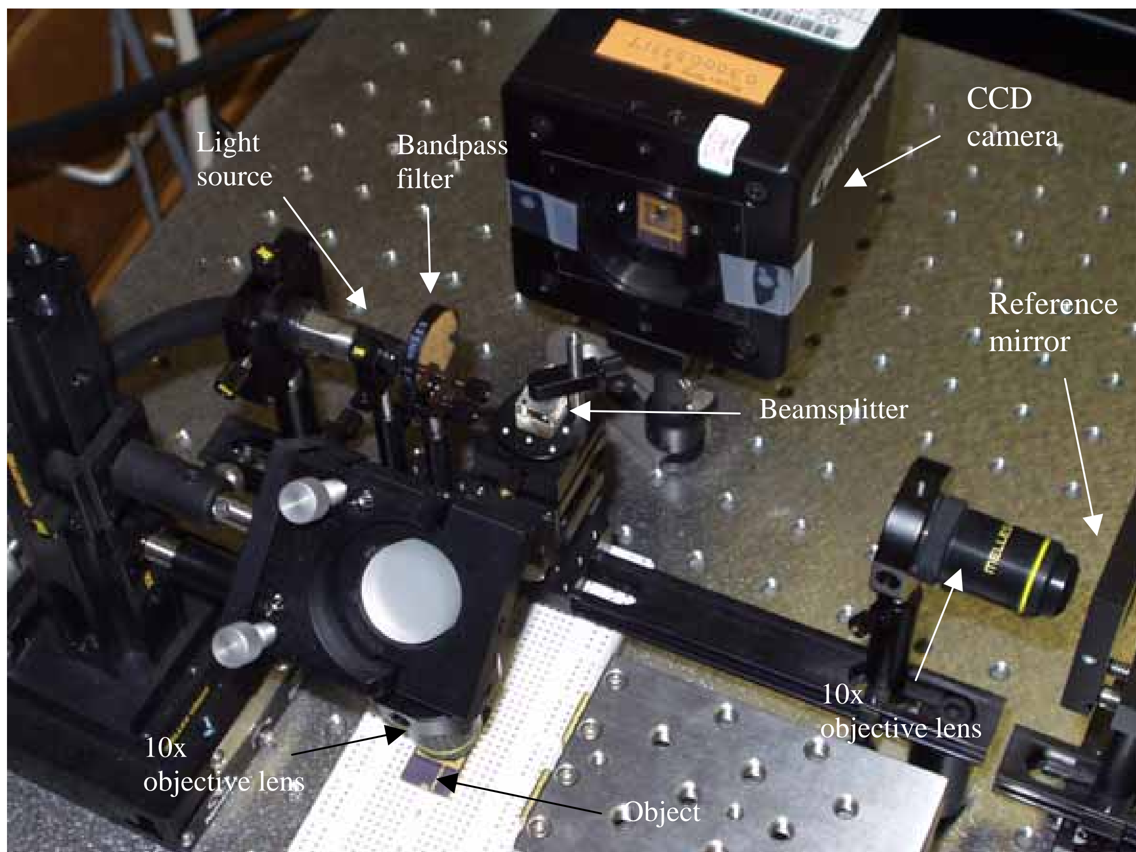

Fig. 5.1. Photograph of measurement set-up

used to measure a translation, rotation, and flatness of micromirror with small size. Fig. 5.1 is

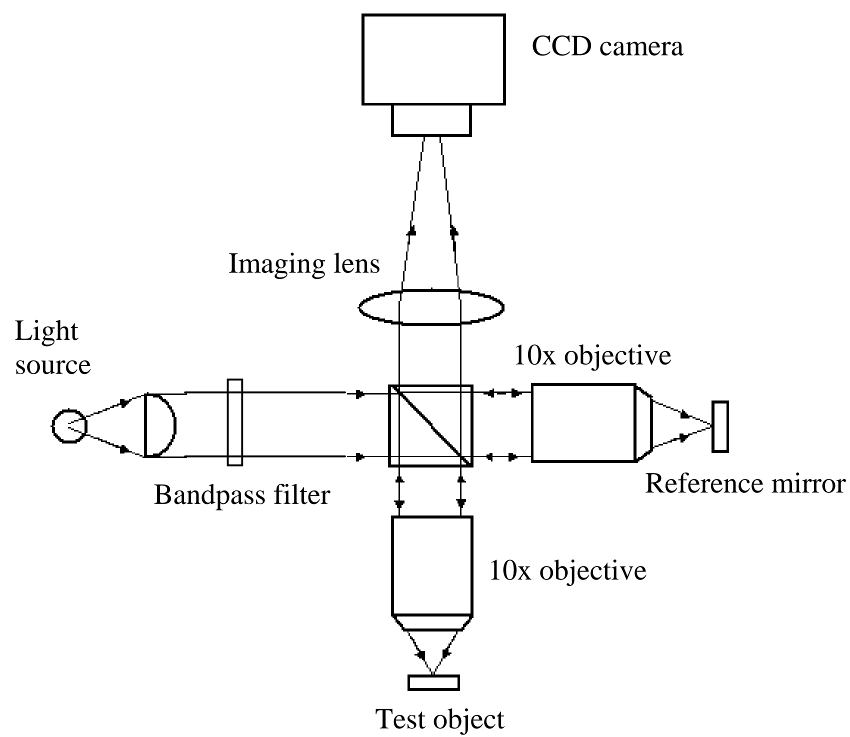

Fig. 5.2. Linnik interferometry to measure translation, rotation and flatness

a photograph of the measurement set-up and Fig. 5.2 is a schematic diagram of the measurement system. A white light passes through a 632nm bandpass filter and is split into reference and object beams, which are focused through each 10x microscope objective. The reference beam is reflected off the reference mirror and returns to the beamsplitter, where it is also reflected to the CCD camera. The object beam is reflected off the device and returns through the beam splitter to the CCD camera, where interference pattern is created with the reference beam. The magnitude of the electrical fields for the reference and object beams can be written as [44]:

$$E_r(x,y) = E_{ro}(x,y)\exp\left(i\left[\frac{2\pi}{\lambda}W_r(x,y) - \omega\, t + \varphi_r\right]\right) \tag{3.16}$$

$$E_m(x,y) = E_{mo}(x,y)\exp\left(i\left[\frac{2\pi}{\lambda}W_m(x,y) - \omega\, t + \varphi_m\right]\right) \tag{3.17}$$

where ω and t represent the angular frequency and traveling time of the electrical wave, λ is the wavelength of the light beam, $W_r(x,y)$ and $W_m(x,y)$ represent the optical paths of the reference and object mirrors respectively, ϕ_r and ϕ_m are the initial phases and $E_{ro}(x,y)$ and $E_{mo}(x,y)$ are the amplitudes of the reference and object fields, respectively. The light intensity produced by two interfering electrical fields can be described as

$$I(x,y) = I_0(x,y)\left\{1 + V(x,y)\cos\left\{k\left[\Delta W(x,y) - \phi\right]\right\}\right\} \tag{3.18}$$

where $I_0(x,y)$ is the average intensity, $V(x,y)$ is the fringe contrast, $\Delta W(x,y)$ is the optical pathlength difference (OPD), k is the wave number ($2\pi/\lambda$), and ϕ ($=\varphi_r - \varphi_m$) is the difference

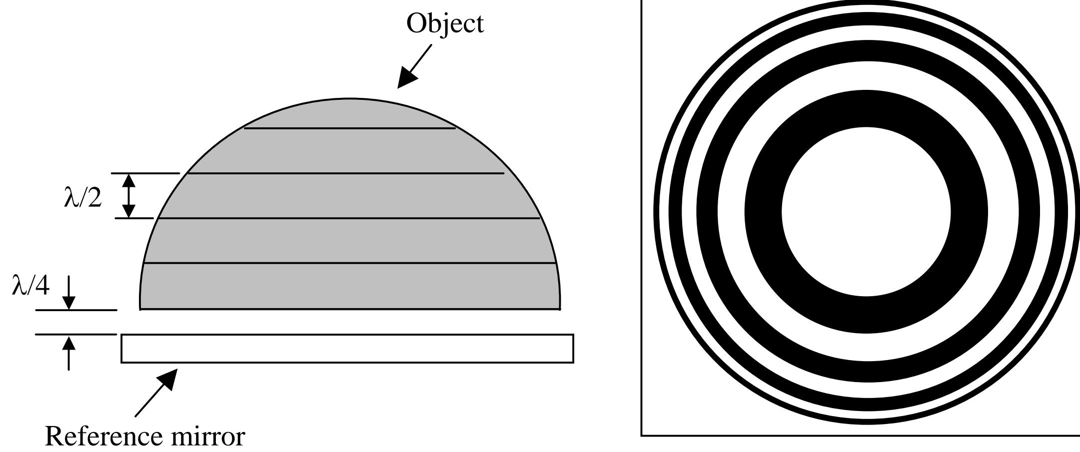

Fig. 5.3. Fringe pattern by a spherical object and reference mirror

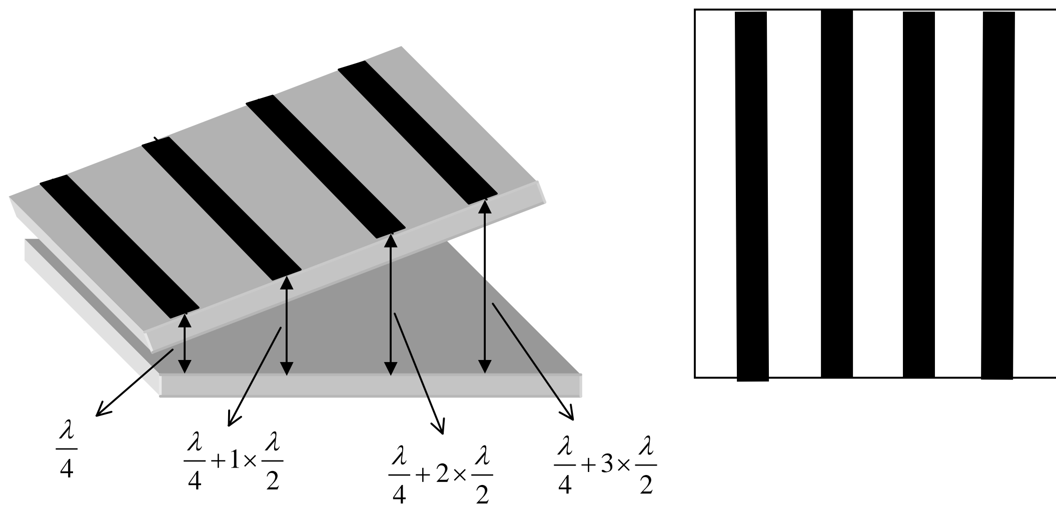

Fig. 5.4. Equally spaced fringes by pre-tilting between the reference and object mirror

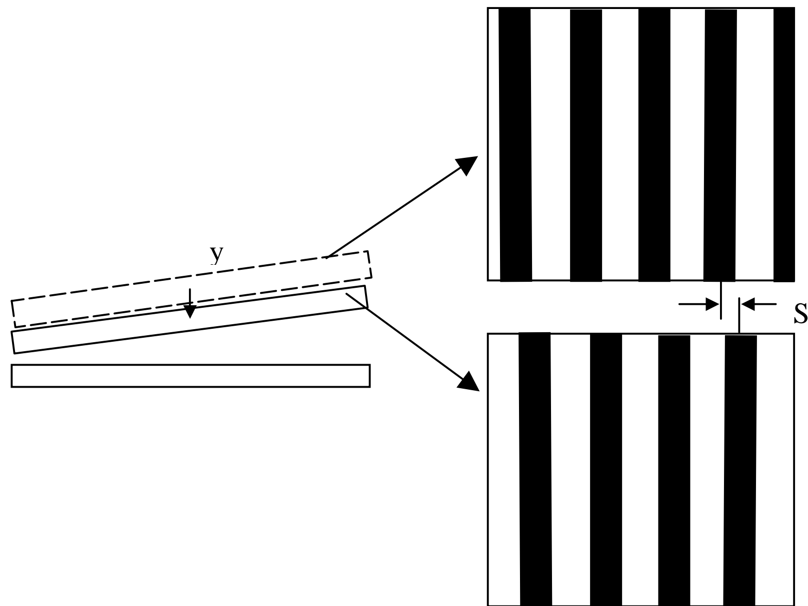

Fig. 5.5. Shifting of fringe pattern by pure translation

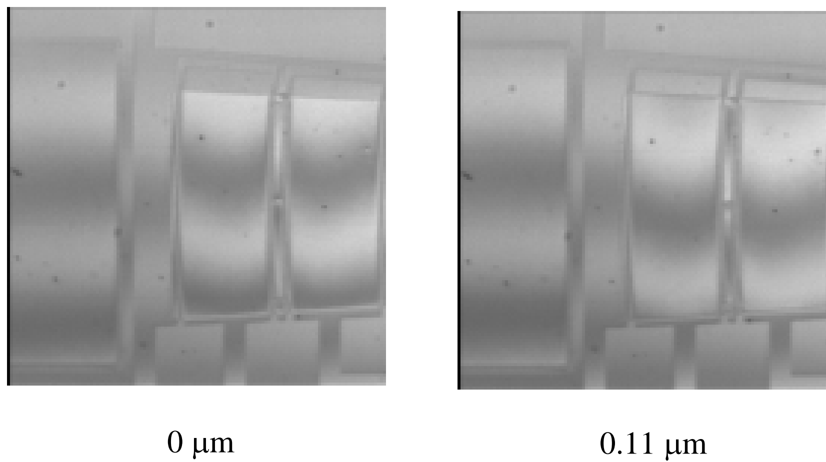

Fig. 5.6. Shifting of the interference fringes by translation

between the reference and object initial phases. The OPD is caused by translation, rotation and flatness of the micromirror. Eq. 5.3 indicates that a fringe pattern with a sinusoidal light intensity distribution will emerge in the superposed area. A fringe pattern is a kind of height contour map that represents every λ/2 height difference. Fig. 5.3 is an example that shows the height contour map of a half of spherical shape.

The pathlength of the object beam increases by twice translation of the mirror. When the mirror translates by λ/2, the interference pattern shifts by one fringe. Thus, translation is measured by determining the amount of shift of the interference patterns. To generate equally spaced fringes as shown in Fig. 5.4, the reference and object should be pre-tilted slightly by a rotational stage upholding the device. When the pitch of interference fringe by pre-tilting of rotation stage is P as shown in Fig. 5.5, the pure translation amount, y is given by

$$y = \frac{\lambda S}{2P} \tag{3.19}$$

where S is the shifting amount of interference fringes. Fig. 5.6 shows the shifting of interference fringes on the micromirror by translation. Measurement accuracy of translational displacement by the suggested measuring method is 11nm.

The angular rotation of the micromirror about a reference mirror is determined by the pitch of the interference fringe and the wavelength of light and is given by

$$\alpha = \arctan\left[\frac{\lambda}{2P}\right] \approx \frac{\lambda}{2P} \tag{3.20}$$

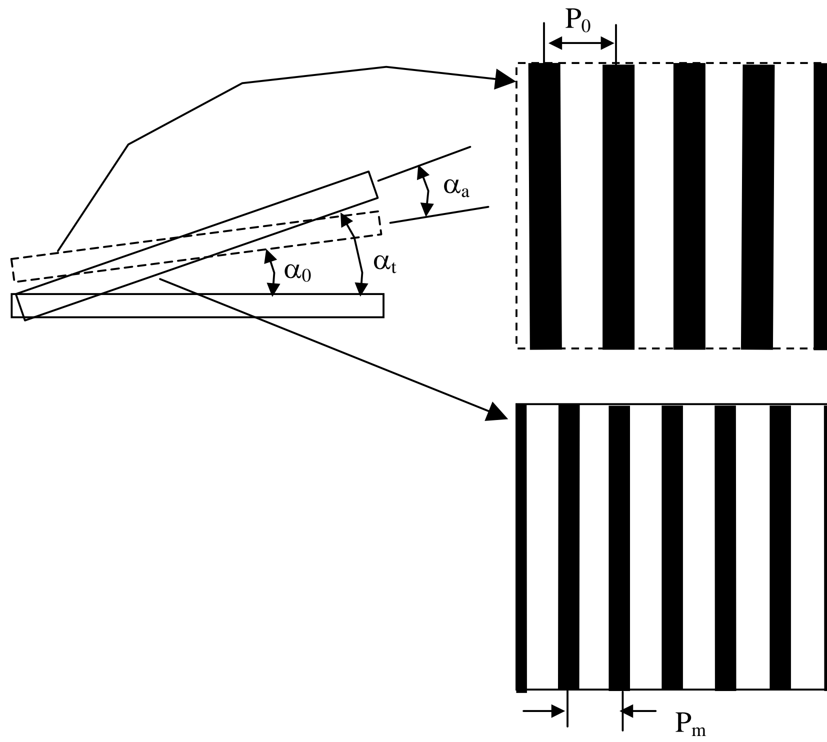

Fig. 5.7. Change of a fringe pitch by rotation of the micromirror

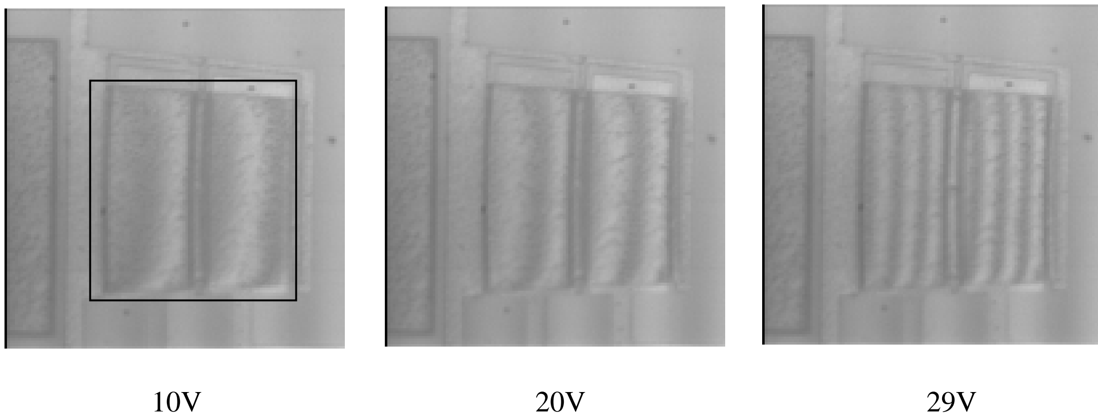

Fig. 5.8. Interference fringes by rotational motions according to the applied voltages

The actual angular rotation, α_a of the micromirror is determined by subtracting the pre-tilted amount from the total angular rotation amount as shown in Fig. 5.7 and is given by

$$\alpha_a = \alpha_t - \alpha_0 \approx \frac{\lambda}{2}\left[\frac{P_o - P_t}{P_t \cdot P_o}\right] \tag{3.21}$$

where P_t is the pitch of interference fringe by the actuated micromirror and P_o is the pitch of interference fringe by pre-tilted micromirror. Fig. 5.8 demonstrates the change of fringe pitch according to the voltage applied to the inside electrode when the outside electrode and ground electrode are at zero volts. Measurement accuracy of rotational displacement by the suggested measuring method is 0.02°.

5.2 Control and package

The MMAL requires DC voltages of 16 channels with 50V range. Each channel should generate independent output simultaneously. In general, a power supply does not support more than 4 channels. Even though 16 channels are possible with several power supplies, it is very expensive to make 16 channels. A D/A converter can have more than 16 channels and each channel output can be controlled independently and simultaneously by PC. By the way, it can not supply more than 12V. Therefore, outputs from D/A converter should be amplified by multi-channel amplifier.

Apex Microtechnology sells the MA32, a 32-channel precision, high voltage op amp for driving capacitive loads. It is an industry precision 32-channel, high voltage monolithic IC that is housed in a 240-pin Quad Flat Pack (QFP). With quiescent current under 325μA per channel, the MA32 drastically reduces the power requirements in systems utilizing multiple high voltage drive channels such as MEMS micromirror arrays. The MA32 has the unique feature of each

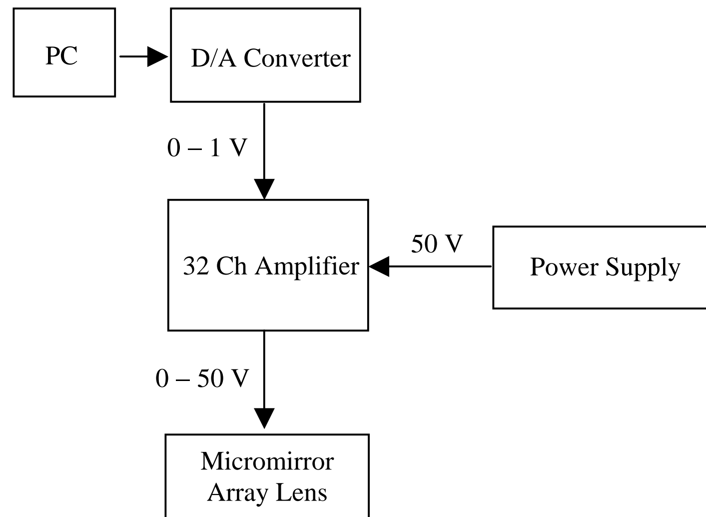

Fig. 5.9. Schematic diagram of multi-channel high voltage control system

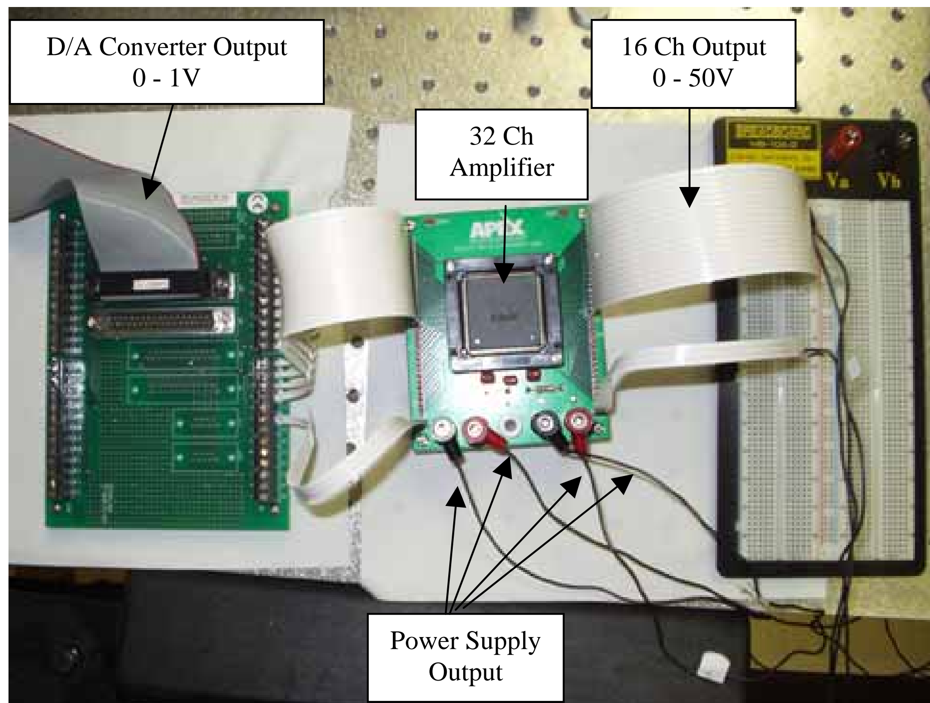

Fig. 5.10. Photograph of control system

channel possessing its own internal biasing to minimize cross talk between channels. The MA32 features a high voltage operation of 220V, and each channel's output voltage can swing up to ±100V with a dual supply and up to 200V with a single supply. Each channel is capable to source/sink up to 700μA and gain of each channel is 50.

Fig. 5.9 and Fig. 5.10 show the control system. Zero to 1 V outputs from 16 channels of a D/A converter were connected to a 32 channels amplifier, MA32 that simultaneously generates 0 to 50V independently. Power supply was also connected with MA32 to supply necessary power.

The MMAL was packaged with a dual-in-line package (DIP). Electrical pads of the MMAL were wired to pads of a DIP by wire bonder and it was sealed with a glass plate as shown in Fig. 5.11. The MMAL packaged by DIP was put on breadboard. DC voltage outputs from MA32 were connected to electrodes of MMAL through breadboard, DIP pads and wires.

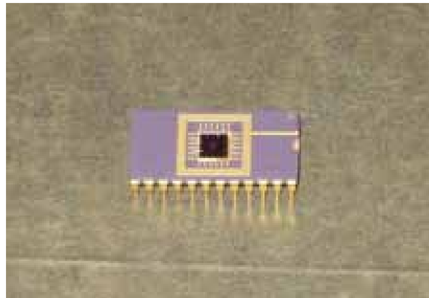

Fig. 5.11. Photograph of MMAL packaged by DIP

CHAPTER VI

RESULTS

6.1 Measurement results

The theoretical behavior of a micromirror was calculated using factors such as the designed spring shapes and dimensions and the modulus of elasticity. Practically, it is hard to find all the factors exactly. Given this uncertainty in the factors, the model will only produce an approximate behavior for the micromirror. However, by changing only the spring constant, the representative curve can be shifted to match the measured data.

Fig. 6.1 is a plot of voltage versus the translation. The measured data is not coincident with

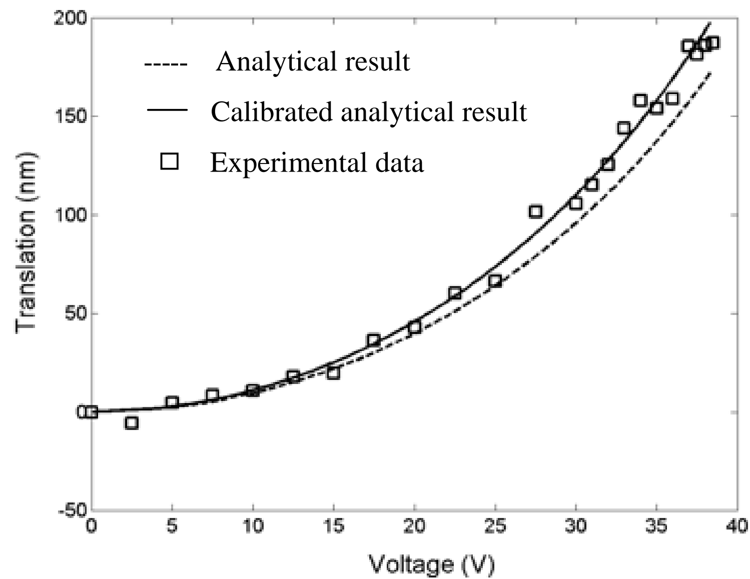

Fig. 6.1. Plot of the voltage versus translation

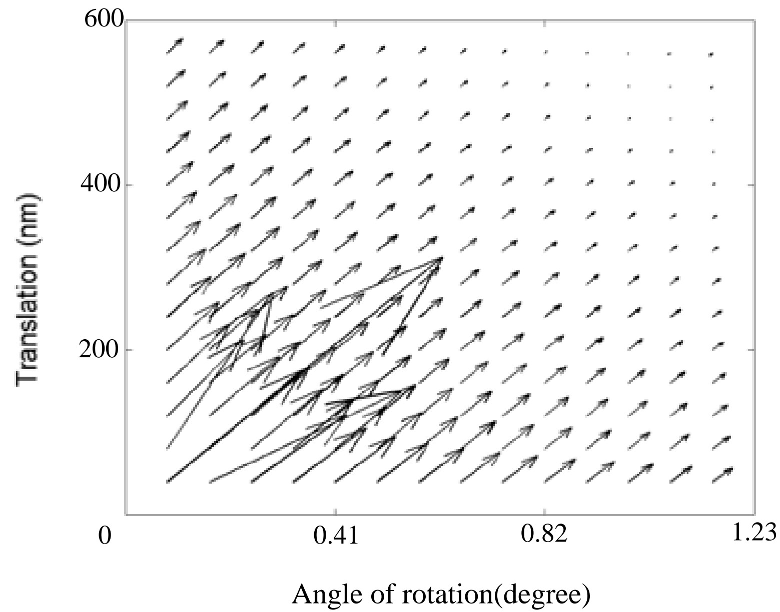

Fig. 6.2. Gradient of the voltage, 3μm gap and a reduced translational spring constant

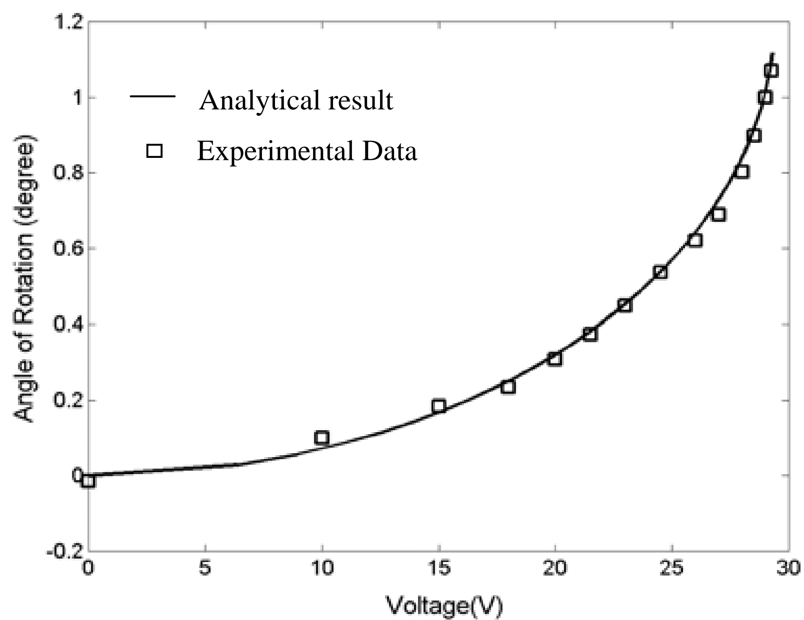

Fig. 6.3. Plot of the voltage versus rotation

analytical curve. By changing only the analytical translational stiffness from 97.8N/m to 85N/m, the analytical curve can be shifted to match the measured data. The measured maximum stable translation is 187nm at 38.5V, which is less than the required translational range, 316nm. The maximum translation is limited by the rotational pull-in instability. The rotational pull-in instability happens before reaching the translational pull-in instability point because torsional stiffness is relatively weaker than translational stiffness. The accuracy of translational motion is 5.8nm. It is only 7% of 79nm, the requirement of translational accuracy. To get sufficient translation, the gap between the electrode and mirror should be increased and the ratio of the torsional stiffness to the translational stiffness should be increased. Fig. 6.2 is a simulated gradient plot of the inside electrode voltage with a 3μm gap and increased ratio of torsional stiffness (3.36*10e-9 N·m) to translational stiffness (4.71N/m). More than 316nm translation and 1.15 degree rotation are possible by increasing the gap and adjusting the stiffness of spring.

Fig. 6.3 is a plot of the voltage of the inside electrode versus the angle of rotation, where the voltage of the outside electrode is zero. The measured data is almost coincident with the analytical curve. Therefore, the analytical torsional stiffness, 1.75×10^{-8}N·m can be used to

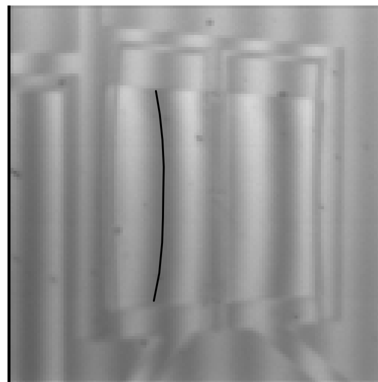

Fig. 6.4. Flatness measurement by fringe deformation

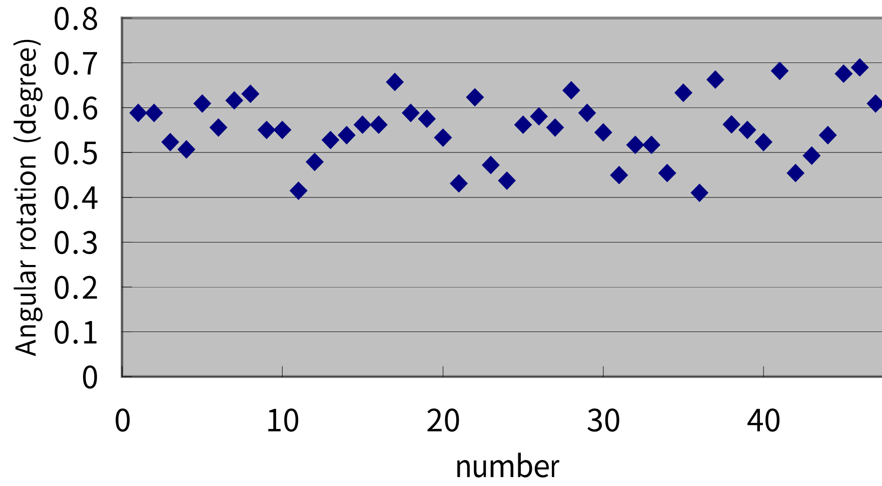

Fig. 6.5. Uniformity of angular rotation, 8th micromirrors, 27V

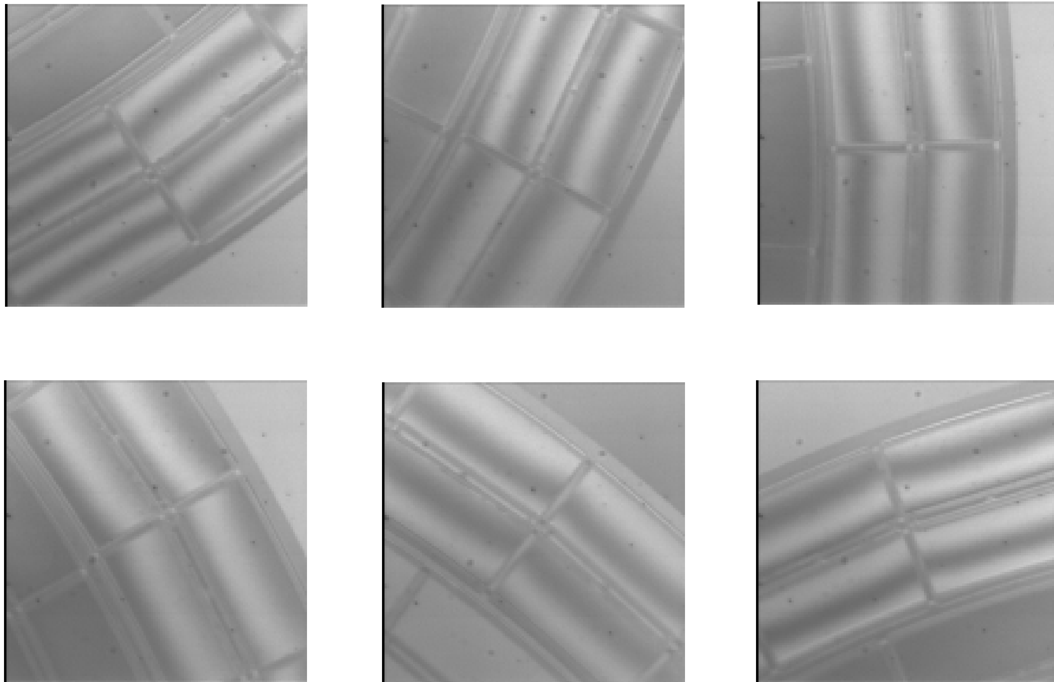

Fig. 6.6. Non-uniformity of micromirror rotation at same radius

predict the calibrated static behavior of a micromirror. The pull-in instability happens at 29.5V, where the maximum stable angle is 0.0188 radians (1.08°). From Eq. (2.2), the maximum practical NA, 0.037 is derived. The accuracy of rotational motion is 0.016°. It is only 17.6% of 0.091°, the requirement of rotational accuracy.

The flatness of the micromirror was measured by the deformational amount of fringe as shown in Fig. 6.4. The surface of the top non-metallized mirror is flat with the sag of 21nm. It is 26.6% of 79nm, the requirement of flatness.

Micromirrors at the same radius should have same rotation because a lens has axis-symmetric structure. Therefore, micromirrors at the same radius were designed to have same shape and same dimensions and to be controlled by same voltage. The angular rotation measured at 8th radius mirrors a large variation as shown in Fig. 6.5 and Fig. 6.6, which shows the fringes by rotation of micromirrors at 8th radius. The standard deviation is 0.072°. It is 79% of 0.091°, the requirement of rotational accuracy. The mean is 0.55° and maximum deviation is 0.14°, which is larger than requirement of rotational accuracy, 0.091°. The main reason for the deviation is the large variation of the spring thickness and width caused by non-uniformity of wet etching to remove the sacrificial layer. Even though the selectivity of HF 48%, etchant of the sacrificial layer is more than 100, long etching time for the releasing of micromirror causes a considerable change of spring thickness and width. In result, it causes a large variation of motion among micromirrors at same radius. Therefore, an etching method with good uniformity such as dry etching is desirable.

Cross-talk occurs due to forces between neighboring electrodes. The force is caused by the fringing effect of neighboring micromirrors, which is a function of perimeter. Fortunately, the cross-talk effect of the micromirror array is negligible because the gap between a bottom electrode and the micromirror, 2μm, is very much smaller than the micromirror size, 100μm. To

check the cross-talk effect, the rotational displacement was measured when 30V was given at neighboring electrodes. In result, the rotational displacement did not happen. It is verified experimentally that cross-talk effect can be ignored for the current micromirror array.

Table. 6.1. Summary of the reasons causing aberration and the rate of aberrations

Aberration reason of MMAL	Rate of aberration	
	$\left(\frac{\sigma}{\lambda/8}\right)\times 100$ %	$\left(\frac{Max}{\lambda/8}\right)\times 100$ %
Insufficient translation		163 %
Accuracy of translation	7 %	
Accuracy of rotation	17.6 %	
Non-uniformity of rotation	79 %	
Flatness		26.6 %

Table. 6.2. Necessary displacement, displacement error and necessary voltages for MMAL with focal length 33mm

Radius	Necessary & possible rotation (degree)	Necessary translation (nm)	Possible translation (nm)	Translation error (nm)	Inside voltage (V)	Outside voltage (V)
1st	0.0726	7.8	7.8	0	19.88	4.99
2nd	0.1641	106	106	0	41.30	30.28
3rd	0.2551	38	38	0	25.30	9.10
4th	0.3641	**120**	**82**	**38**	31.60	20.00
5th	0.4392	**37**	**40**	**3**	28.30	0
6th	0.5274	**108**	**56**	**52**	28.80	6.00
7th	0.6178	**15**	**65**	**50**	28.90	0
8th	0.7082	75	75	0	30.30	0

Table 6.1 summarizes the reasons causing aberration and the aberration rate by each reason from the measured result. Among them, aberrations by insufficient translation and non-uniformity of rotational motion are critical. To extend the translation range, the gap between a bottom electrode and the micromirror should be larger than 2μm and the non-uniformity of rotational motion should be improved by using dry etching or wet etching with better uniformity.

6.2 Optical performance

Aberration by insufficient translation was inevitable because the MMAL was fabricated by the MUMPs process, which restricts the gap between electrode and micromirror to be 2μm. To minimize the insufficient translation effect, a MMAL requiring each micromirror to have a relatively small translation was generated. The focal length of the lens is 33mm. A feasible imaging performance of the proposed lens is estimated with the lens. Table 6.2 shows the necessary rotation and translation to make the MMAL with focal length 33mm and aberration by insufficient translation.

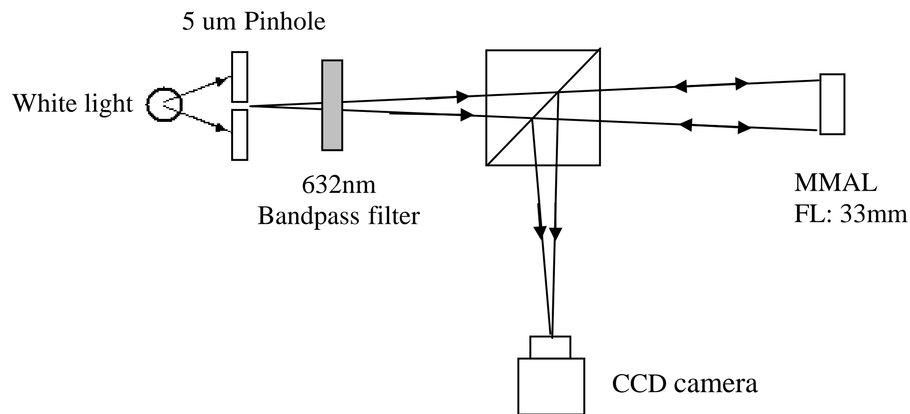

Fig. 6.7. Set-up for spot diameter measurement

There are many methods to evaluate the optical performance. Several commonly accepted criteria for image evaluation are Spot Diameter, Blur-Spot Size, Rayleigh Quarter-Wave Limit, Strehl Ratio, Depth of Focus, etc. Among them, Spot Diameter is used to evaluate the optical performance of the MMAL because it is a common evaluation criterion and determines the resolution of image.

Fig. 6.7 shows an experimental set-up to measure a spot diameter. It is measured to test the focusing quality. A point source was made by 5μm pinhole illuminated by monochromatic light source, which is generated by 632nm bandpass filter. At the experimental set-up, the focal length of MMAL is 33mm and the magnification of the imaging system is 1. The numerical aperture (NA) is 0.0136 at given imaging system. Fig. 6.8 shows the image of a 5μm point source, which has a 34.8μm diameter. It is 8.75% larger than 32μm, spot diameter of 5μm

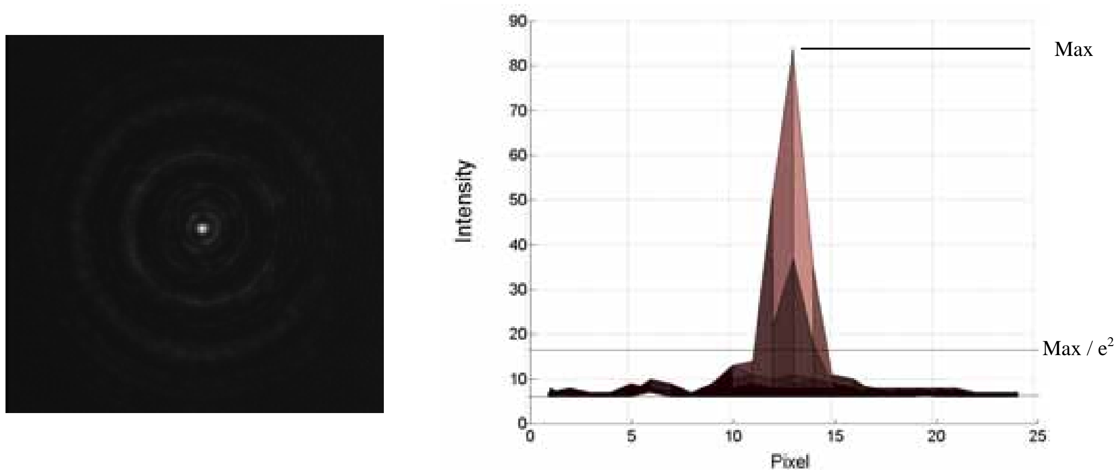

Fig. 6.8. Spot diameter by MMAL with NA 0.0136

diameter point source by diffraction-limited lens with NA 0.0136. Fig. 6.9 is an image of real object imaged by the MMAL. Visibility of the image is low. Main reasons of the blurring of spot diameter and the low visibility of image are non-uniformity of angular rotation at same radius, insufficient translation range and low reflectivity of polysilicon, which is a material of micromirror surface. Light reflected by surrounding surfaces of a mirror plate causes a significant noise because reflectivity of a mirror plate is similar with reflectivity of surrounding surface. The noise degrades the visibility of image. Besides above reasons, approximation, flatness, rotational and translational error also degrade optical performance.

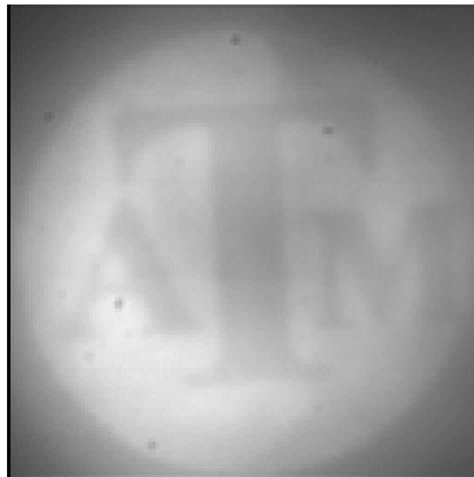

Fig. 6.9. Image of real object imaged by the MMAL

CHAPTER VII

CONCLUSIONS

A fast response micromirror array lens(MMAL) was designed, fabricated and test using the Fresnel lens principle, which uses an array of electrostatically actuated micromirrors. The focal length of the lens can be rapidly changed by controlling both the rotation and translation of electrostatically actuated micromirrors. The lens has a fast response time in the order of several tens KHz, large focal length variation. Also, large diameter lens is possible without losing of optical performance.

The designed lens diameter is 1.8mm, and a polar array of micromirrors with fan shape was used. At a given radial position, each mirror has the same shape because the lens is axis-symmetric. Each mirror is 100μm wide in the radial direction, and the circumferential dimension is specified such that each mirror has an area of 10,000μm^2. The mirror size and shape at each radial position are designed to increase the effective area for optical efficiency and to decrease the approximation error between the ideal curved shape of a reflective lens and flat surface shape of mirror.

Each mirror is translated to adjust the optical path length (OPL), and the required translation range is $\lambda/2$. The rotation angle of each micromirror is controlled to converge the rays. The required range of angle depends on the required maximum numerical aperture (NA) of the lens.

The point spread function (PSF) of an imaging system using the MMAL was simulated. The spot diameter by MMAL is approximately 22μm, whereas the spot diameter by a diffraction-limited lens is 21.4μm for the NA of 0.018. Thus, the resolution of the MMAL almost same with

a diffraction-limited lens. The simulated Strehl ratio, which is the ratio of the PSF maximum intensity to the maximum intensity for a theoretical diffraction-limited PSF is 31.2%.

The translational and torsional stiffness were calculated to find elastic recovery force and torque, and electrostatic force and torque were calculated by regarding plate as being composed of an infinite number of infinitesimally-small capacitors. The static behavior of the micromirror was determined by two static equations, force equation and moment equation, with two variables, translational displacement (y) and rotational displacement (α) at equilibrium.

Electrostatic actuators undergo the classical pull-in instability when the electric force exceeds the elastic force. For pure translation, there is no instability for a translation less than 666nm, 1/3 of the gap between the electrode and mirror. However, a mirror having two coupled degrees of freedom has a different instability point. Analytical solution showed that rotational pull-in instability occurs before reaching a translation of 316nm.

The designed MMAL is successfully fabricated with MUMPs® surface micromachining process. The final layer in the MUMPs process is a 0.5μm metal layer. But the metal layer causes a deformation of micromirror by thermal residual stress. Therefore, the deposited metal is removed thoroughly using lift-off.

Linnik interferometry was used to measure a translation, rotation, and flatness of a fabricated micromirror. Translation was measured by determining the amount of shift of the interference patterns. The angular rotation of micromirror about a reference mirror was determined by the pitch of interference fringe.

The MMAL requires DC voltages of 16 channels with a 0 to 50V range. Each channel should generate independent output simultaneously. Zero to 1 V outputs from 16 channels of a D/A converter were connected to a 32 channels amplifier, MA32 that simultaneously generates 0 to

50V independently. The MMAL packaged by DIP was putted on breadboard. DC voltage outputs from MA32 were connected to electrodes of MMAL through breadboard, DIP and wires.

Translational stiffness was calibrated with measured data from 97.8N/m to 85N/m. The maximum stable translation is 187nm at 38.5V. It is less than the required translational range, 316nm. The accuracy of translational motion is 5.8nm.

The measured rotation data was almost coincident with analytical curve. The measured torsional stiffness is 1.75×10^{-8}N·m, which is same with analytical value. Rotational pull-in instability happened at 29.5V. The maximum stable angle is 0.0188 radians (1.08°). Therefore, the maximum practical NA is 0.0377. The accuracy of rotational motion is 0.016°.

The surface for the top non-metallized mirror is flat with the sag of 21nm. Uniformity of 8th micromirrors' rotation is 0.072°, which is 79% of 0.091°, the requirement of rotational accuracy. The maximum deviation is 0.14°, which is larger than requirement of rotational accuracy, 0.091°. Therefore, etching method with good uniformity such as dry etching is desirable. Cross-talking effect of the designed micromirror array can be ignorable.

Spot diameter of point source was measured to test focusing quality. Measured spot diameter is 34.8μm, which is 8.75% larger than 32μm, spot diameter size by diffraction-limited lens. Finally, real object was imaged by MMAL. Visibility of the image is low. Main reasons of blurring of spot diameter and low visibility of image are non-uniformity of angular rotation at same radius, insufficient translation range and low reflectivity of polysilicon, material of micromirror surface.

The designed MMAL has a relatively lower optical performance than conventional refractive lens by insufficient translation range, non-uniformity, low reflectivity of micromirror surface and other reasons. The reasons should be improved or removed to make a MMAL with similar or better optical performance than a conventional lens.

REFERENCES

[1] E.C. Tam, Smart electro-optical zoom lens, Opt. Lett. 17 (1992) 369-371.

[2] T. Kaneko, K. Ohba, N. Mitsumoto, and N. Kawahara, Quick response dynamic focusing lens using multi-layered Piezoelectric bimorph actuator, Proc. SPIE 4075 (2000) 24-31.

[3] M. Hain, R. Glockner, S. Bhattacharya, D. Dias, S. Stankovic, T. Tschudi, Fast switching liquid crystal lenses for a dual focus digital versatile disc pickup, Opt. Commun. 188 (2001) 291-299.

[4] L. G. Commander, S.E. Day, D.R. Selviah, Variable focal length microlenses, Opt. Commun. 177 (2000) 157-170.

[5] N. Suguira and S. Morita, Variable focus liquid-filled optical lens, Appl. Opt. 32 22 (1993) 4181–4186.

[6] C.B. Gorman, H.A. Biebuyck and G.M. Whitesides, Control of the shape of liquid lenses on a modified gold surface using an applied electric potential across a self-assembled monolayer, Langmuir 11 (1995) 2242–2246.

[7] E. Saul, Variable focus lens with internal refractive surface, US Patent No. 2,004,001,180, 2004.

[8] M. Chang, Total internal reflection lens, Appl. Opt. 24 (9) (1985) 1256–1259.

[9] T. Shibaguchi and H. Funato, Lead-lanthunum zirconate-titanate (PLZT) electro-optic variable focal length lens with stripe electrodes, Jpn. J. Appl. Phys. 31 (9B) (1992) 3196–3200.

[10] I.C. Khoo, S.T. Wu, Optics and Nonlinear Optics of Liquid Crystals, 1st edn., World Scientific Publishing, Singapore, (1993) 160–193.

[11] A. Yariv, Quantum Electronics, 3rd edn., Wiley, New York, (1989).

[12] D. Berreman, Variable focus liquid crystal lens system, US Patent No. 4,190,330, 1980.

[13] S. Sato, Liquid crystal lens-cell with variable focal length, Jpn. J. Appl. Phys. 18 (1979) 1679–1684.

[14] K. Tomita, Scanning optical apparatus, US Patent No. 5,130,839, 1992.

[15] K. Nishioka, Automatic focusing device using liquid crystal lens, Jpn. Patent No. 61-156228, 1986.

[16] S. Nose, S. Masuda and S. Sato, Optical properties of a liquid crystal microlens with a symmetric electrode structure, Jpn. J. Appl. Phys. 30 (12b) (1991) 2110–2112.

[17] S. Masuda, S. Fujioka, M. Honma, T. Nose and S. Sato, Dependence of optical properties on the device and material parameters in liquid crystal microlenses, Jpn. J. Appl. Phys. 35 (9A) (1996) 4668–4672.

[18] S.T. Kowel, D.S. Cleverly and P.G. Kronreich, Focusing by electrical modulation of refraction in a liquid crystal cell, Appl. Opt. 23 (2) (1984) 278–289.

[19] N.A. Riza and M.C. DeJule, Three-terminal adaptive liquid-crystal lens device, Opt. Lett. 19 (14) (1994) 1013–1015.

[20] A.F. Naumov, M.Yu. Loktev, I.R. Guralnik and G. Vdovin, Liquid-crystal adaptive lenses with modal control, Opt. Lett. 23 (1998) 992–994.

[21] P.W. McOwan, M.S. Gordon and W.J. Hossack, A switchable liquid crystal binary Gabor lens, Opt. Commun. 103 (1993) 189–193.

[22] J.S. Patel and K. Rastani, Electrically controlled polarization-independent liquid-crystal Fresnel lens arrays, Opt. Lett. 16 (7) (1991) 532–534.

[23] G. Williams, N. Powell, A. Purvis and M.G. Clark, Electrically controllable liquid crystal Fresnel lens, Proc. SPIE 1168 (1989) 352–357.

[24] S. Sato, A. Sugiyama and R. Sato, Variable-focus liquid-crystal Fresnel lens, Jpn. J. Appl. Phys. 24 (8) (1985) 626–628.

[25] J. Eschler, S. Dickmann, D.A. Mlynski and H. Molsen, Fast adaptive lens based on deformed helix ferroelectric liquid crystal, Ferroelectrics 181 (1996) 21–28.

[26] T. Lin, Implementation and characterization of a flexure-beam micromechanical spatial light modulator, Optical Engineering 33 (11) (1994) 3643-3648.

[27] H. Kim, J. Kim and H. Shin, A laser-based 2-dimensional angular deflection measurement system for tilting microplates, Sensors and Actuators 86 (2000) 141-147.

[28] M. Fischer, M. Giousour, J. Schaepperle, D. Eichner, M. Weinmann, W. vonMunch, F. Assmus, Electrostatically deflectable polysilicon micromirrors - dynamic behaviour and comparison with the results from FEM modeling with ANSYS, Sensors and Actuators A 67 (1998) 89-95.

[29] S. Chung, Y. Kim, Design and fabrication of 10×10 micro-spatial light modulator array for phase and amplitude modulation, Sensors and Actuators A 78 (1999) 63-70.

[30] T. Veijola, H. Kuisma, J. Lahdenpera, T. Ryhanen, Equivalent-circuit model of the squeezed gas film in a silicon accelerometer, Sensors and Actuators A 48 (1995) 239-248.

[31] M. K. Andrews, G.C. Turner, P.D. Harris, A resonant pressure sensor based on a squeeze film of gas, Sensors and Actuatros A 36 (1993) 219-226.

[32] J. J. Blech, On isothermal squeeze films, J. Lubrication Technol.105 (1983) 615-620.

[33] M. A. Michalicek, J. H. Comtois, and H. K. Schriner, Geometry versus optical performance of micromirrors and arrays, Proc. SPIE 3440 (1998) 140-147.

[34] M. A. Michalicek and V. M. Bright, Development of advanced micromirror arrays by flip-chip assembly, Proc. SPIE 4561 (2001) 102-113.

[35] M. A. Michalicek and V. M. Bright, Fabrication of five-level, ultra-planar micromirror arrays by flip-chip assembly, Proc. SPIE 4561 (2001) 293-304.

[36] M. A. Michalicek, V. M. Bright and J. H. Comtois, Design, fabrication, modeling, and testing of a surface-micromachined micromirror device, Proc. of the ASME Dyanmic Systems and Control Division, DSC 57 (2) (1995) 981-988.

[37] X.M. Ahang, F.S. Chau, C. Quan, Y.L. Lam, A.Q. Liu, A study of the static characteristics of a torsional miromirror, Sensor and Actuator A 90 (2001) 73-81.

[38] J. E. Lin, F. S.J. Michael, and A. G. Kirk, Investigation of improved designs for rotational micromirrors using Multi-User MEMS Processes, Proc. SPIE Vol. 4407 (2001) 202- 213.

[39] O. Degani and Y. Nemirovsky, Design considerations of rectangular electrostatic torsion actuators based on new analytical Pull-in expressions, Journal of Microelectromechanical Systems, Vol. 11, No. 1 (2002) 20-26.

[40] R. Nadal-Guardia, A. Dehe, R. Aigner, and L. M. Castaner, Current drive methods to extend the range of travel of electrostatic microactuators beyond the voltage Pull-In point, Journal of Microelectromechanical Systems, Vol. 11, No. 3, (2002) 255-263.

[41] D. M. Burns and V. M. Bright, Designs to improve polysilicon micromirror surface topology, Proc. SPIE 3008 (1997) 100-110.

[42] R. Nasby, J. Sneigowski, J. Smith, S. Montague, C. Barron, W. Eaton, and P. MeWhorter, Application of chemical-mechanical polishing to planarization of surface-micromachined devices, Technical Digest, Solid State Sensors and Actuators Workshop (Hilton Head, SC, 3-6 June 1996), 48-53.

[43] C. Kim, J. Y. Kim, B. Sridharan, Comparative evaluation of drying techniques for surface micromachining, Sensors and Actuators A 64 (1998) 17-26.

[44] R. D. Guenther, Modern Optics, Wiley, New York, 1990

APPENDIX A

DIFFRACTION IMAGERY (Born and Wolf, 1964)

A-1 THE POINT-SPREAD FUNCTION; THE DIFFRACTION INTEGRAL

The exact point-spread function P (y, z) of an image (as contrasted to the approximate geometrical function derived from ray tracing) is given by

$$P(y,z) = \left|A(y,z)\right|^2 \qquad \text{(A.1.1)}$$

where A(y, z) is the complex phase amplitude of the wavefront emerging from the optical system, given by

$$A\left(y,z\right) = \int\int_{-\infty}^{\infty} B\left(u,v\right)\exp\left[-i\frac{2\pi}{\lambda}\phi\left(u,v\right)\right]\exp\left(i\frac{2\pi}{\lambda}\frac{uy+vz}{F}\right)dudv \qquad \text{(A.1.2)}$$

where, y, z = coordinates in image plane normal to principal ray

u, v = coordinates in exit pupil normal to principal ray

λ = wavelength

B(u, v) = amplitude factor proportional to square root of flux density, i.e., transmission, at point (u, v) in pupil; B(u, v) = 0 outside pupil

ϕ(u, v) = wave-aberration function ; ϕ(u, v) = OPD of the ray through point (u, v)

F = radius of reference sphere

I = imaginary $(-1)^{1/2}$

The terms B(u, v) and $\exp[-(i2\pi/\lambda)\phi(u, v)]$ are often combined and referred to as the pupil function of the system. Equation(A.1.2) is sometimes written to include a focusing term, $\exp[i\pi x(u^2+v^2)/\lambda F^2]$.

A-2 THE DIFFRACTION IMAGE

If the pupil function is a constant, i.e., if the transmission of the system is uniform over the (circular) aperture and the system is aberration-free, the illuminance distribution in the image becomes

$$P(y,z)=\pi\left(\frac{NA}{\lambda}\right)^2 P_t\left[\frac{2J_1(m)}{m}\right]^2 = I_0\left[\frac{2J_1(m)}{m}\right]^2 \tag{A.2.1}$$

where NA = n·sin(U) is the numerical aperture of the system, $J_1(\cdot)$ is the first-order Bessel function

$$J_1(x)=\frac{x}{2}-\frac{(x/2)^3}{1^2 2}+\frac{(x/2)^5}{1^2 2^2 3}-\cdots\cdots \tag{A.2.2}$$

P_t is the total power in the point image, and m is the normalized radial coordinate

$$m=\frac{2\pi}{\lambda}NA(y^2+z^2)^{1/2}=\frac{2\pi}{\lambda}NA\cdot s \tag{A.2.3}$$

The fraction of the total power falling within a radial distance s_0 of the center of the pattern is given by $1-J_0^2(m_0)-J_1^2(m_0)$, where $J_0(\cdot)$ is the zero-order Bessel function

$$J_0(x)=1-\left(\frac{x}{2}\right)^2+\frac{(x/2)^4}{1^2 2^2}-\frac{(x/2)^6}{1^2 2^2 3^2}+\cdots\cdots \tag{A.2.4}$$

Equation (A.2.4) shows the appearance of the diffraction pattern. The pattern consists of a circular patch of light (the Airy disk) surrounded by rings of rapidly decreasing intensity.

Table A.2.1 indicates the size and distribution of energy in the pattern for a circular aperture.

Table A.2.1 Distribution of Energy in the Diffraction Pattern at the Focus of a Perfect Lens as a Function of the Distance Z from the Pattern Center (Smith, 1965)

	Circular aperture		
Ring (or band)	Z	Peak illumination	Energy in ring, %
Central maximum	0	1.0	83.9
First dark ring	$\frac{0.61\lambda}{n \cdot \sin U}$	0.0	......
First bright ring	$\frac{0.82\lambda}{n \cdot \sin U}$	0.017	7.1
Second dark ring	$\frac{1.12\lambda}{n \cdot \sin U}$	0.0	......
Second bright ring	$\frac{1.33\lambda}{n \cdot \sin U}$	0.0041	2.8
Third dark ring	$\frac{1.62\lambda}{n \cdot \sin U}$	0.0	......
Third bright ring	$\frac{1.85\lambda}{n \cdot \sin U}$	0.0016	1.5
Fourth dark ring	$\frac{2.12\lambda}{n \cdot \sin U}$	0.0	......
Fourth bright ring	$\frac{2.36\lambda}{n \cdot \sin U}$	0.00078	1.0
Fifth dark ring	$\frac{2.62\lambda}{n \cdot \sin U}$	0.0	......

VITA

Personal Data

Name	Gyoungil Cho
Present Address	2450 Daphne Pl #223, Fullerton, CA, 92833

Education

3/1991 – 2/1995	B.S., Department of Machine Design Sung Kyun Kwan University Seoul, Korea
3/1995 – 2/1997	M.S., Department of Mechanical Engineering Korean Advanced Institute of Science and Technology Daejon, Korea
8/1998 – 12/2000	Ph.D., Department of Mechanical Engineering University of Illinois at Chicago IL, USA
01/2001 – present	Ph.D., Department of Aerospace Engineering Texas A&M University TX, USA